



저작자표시-비영리-변경금지 2.0 대한민국

이용자는 아래의 조건을 따르는 경우에 한하여 자유롭게

- 이 저작물을 복제, 배포, 전송, 전시, 공연 및 방송할 수 있습니다.

다음과 같은 조건을 따라야 합니다:



저작자표시. 귀하는 원저작자를 표시하여야 합니다.



비영리. 귀하는 이 저작물을 영리 목적으로 이용할 수 없습니다.



변경금지. 귀하는 이 저작물을 개작, 변형 또는 가공할 수 없습니다.

- 귀하는, 이 저작물의 재이용이나 배포의 경우, 이 저작물에 적용된 이용허락조건을 명확하게 나타내어야 합니다.
- 저작권자로부터 별도의 허가를 받으면 이러한 조건들은 적용되지 않습니다.

저작권법에 따른 이용자의 권리는 위의 내용에 의하여 영향을 받지 않습니다.

이것은 [이용허락규약\(Legal Code\)](#)을 이해하기 쉽게 요약한 것입니다.

[Disclaimer](#)

이학박사 학위논문

**Angle-Resolved Photoemission
Spectroscopy on Itinerant Electrons in a
2D Electride and 3D Perovskite Oxides**

2 차원 전자화물 및 3 차원 산화물 페로브스카이트 내
유동 전자에 대한 각분해 광전자 분광학 연구

2018 년 8 월

서울대학교 대학원

물리천문학부

오 지 섭

**Angle-Resolved Photoemission
Spectroscopy on Itinerant Electrons in a
2D Electride and 3D Perovskite Oxides**

Ji Seop Oh

Supervised by
Professor Tae Won Noh

A Dissertation submitted to the Faculty of Seoul National
University in Partial Fulfillment of the Requirements for the
Degree of Doctor of Philosophy

August 2018

*Department of Physics and Astronomy
Graduate School
Seoul National University*

Abstract

Itinerant electrons in solids play an important role since they determined physical properties such as conduction or magnetism. In some simple systems such as alkali or alkaline-earth metals in which interactions between electrons are negligible, it is relatively easy to study relation between electronic structures and physical properties by both experiments and theory. However, if the interactions or correlations become important, studying electronic structure of such systems is complicated since conventional band theory fails to describe correct electronic structures. In this dissertation, we studied three different itinerant electron systems by photoemission spectroscopy to overcome the limitations. Each work had experimental and theoretical difficulties at the moment starting the experiments. We tried to resolve the difficulties by adopting user facilities and state-of-the-art experimental techniques.

For the first part, we presented the first study of electronic structures for an electride Ca_2N by angle-resolved photoemission spectroscopy (ARPES). An electride is a system in which electrons themselves behave as anions. Adopting synchrotron radiation, we could perform ARPES using various photon energies. It determines k_z dispersions of the electronic structure of Ca_2N , and we found Fermi momenta k_F was almost constant with respect to k_z values. It directly revealed that low-energy excitation governed by the electronic structure should follow quasi-two-dimensional behavior, which was originally suggested by density functional theory (DFT) calculations. Such good agreement also proved that physical

properties related with electronic structures would be consistent with those predicted from DFT calculations. Hence, we provided first experimental evidence for the existence of quasi-two-dimensional anionic excess electrons in Ca_2N .

In the second part, we investigated possible surface metallic states predicted by DFT calculations on BiO_2 -terminated BaBiO_3 thin films. We used an up-to-date *in-situ* core-level photoemission and ARPES systems to study electronic structures of BaBiO_3 thin films. By analyzing angle-dependent Bi $4f$ and Ba $3d$ core-level spectra, we found that our BBO films had BiO_2 termination, which suited the prerequisite for realizing surface metallic states. We also measured momentum-resolved valence band spectra and found our results were consistent with the previous report. Contrary to the theoretical prediction, we did not find any signature of surface metallic states. We studied possible surface states in detail using *in-situ* K evaporation on our BaBiO_3 films, and revealed surface states located -3.8 eV below the Fermi level. We proposed that electronic structure studies for BaBiO_3 is delicate and need sophisticated methods.

As the last part of this dissertation, we studied three-dimensional electronic structure of SrRuO_3 (SRO) single crystals. We determined the inner potential of SRO single crystals for the first time. We also measured the band dispersions on high symmetry planes and opened a way to cross-check theoretical electronic structures of SRO, which has not been accomplished during last 20 years. From temperature dependence of a band dispersion, we found that the ferromagnetic exchange splitting of SRO decreased when temperature rose up. However, it did not become zero at the T_C , and remained as finite values. We suggested that this finite exchange splitting above T_C indicates existence of short-range magnetic

order above T_C and supported dual nature of itinerant/localized magnetism in SRO.

Keywords: itinerant electrons, electronic structures, electride, 2DEG, perovskite, itinerant magnetism, ARPES.

Student number: 2012-20373

Abstract	i
List of figures	ix
1 Introduction	1
1.1 Free (itinerant) electrons in solids and band structures.....	1
1.2 Photoemission spectroscopy (PES) and angle-resolved photoemission spectroscopy (ARPES)	5
1.2.1 Basic aspects of photoemission kinematics	5
1.2.2 The three-step model	8
1.3 Outline of the thesis	11
2 Direct Evidence for 2D Anionic Excess Electrons in an Electride Ca₂N	15
2.1 Introduction	15
2.2 Methods	20
2.3 Results and discussion	23
2.3.1 Fermi surface of Ca ₂ N	23
2.3.2 Band dispersions of Ca ₂ N	26
2.3.3 Orbital characters of the valence band	29
2.4 Conclusion	31
3 Absence of Metallic Surface States in BiO₂-Terminated BaBiO₃ Thin Films	37
3.1 Introduction	37

3.2	Methods	41
3.3	Results and discussion	43
3.3.1	Angle-dependent x-ray photoelectron spectroscopy.....	43
3.3.2	The experimental and simulated spectral-weight ratios between Bi $4f_{7/2}$ and Ba $3d_{5/2}$	46
3.3.3	Constant energy surfaces of BBO	48
3.3.4	Band dispersions of BBO	49
3.3.5	<i>in-situ</i> K dosing onto a BBO thin film	52
3.3.6	Absence of a metallic surface state: oversimplified band calculations .	55
3.4	Conclusion	57
4	Spectroscopic Investigation on Itinerant/Local Magnetism in SrRuO₃	61
4.1	Introduction	61
4.2	Methods	65
4.3	Results and discussion	67
4.3.1	k_z dispersion of the electronic structure of SRO	67
4.3.2	Fermi surfaces of SRO	69
4.3.3	Band dispersions of SRO	72
4.3.4	Temperature and polarization dependence of Fermis surfaces of SRO	74
4.3.5	Exchange splitting and its temperature evolution	78
4.4	Conclusion	82

5 Conclusion 85

Appendix: Manifestations of Quasi-Two-Dimensional Metallicity in a Layered Ternary Transition Metal Chalcogenide Ti_2PTe_2 89

Publication list 103

국문 초록 (Abstract in Korean) 105

감사의 글 (Acknowledgement) 109

List of figures

Figure 1.1 Figure 1.1 Fermi surfaces formed by itinerant and localized electrons. Adopted from [8].

Figure 1.2 A schematic on (angle-resolved) photoemission spectroscopy. Adopted from [8].

Figure 1.3 A schematic diagram of photoemission energetics. Adopted from [10].

Figure 2.1 Crystal Structure of C12A7. Initially cavities in C12A7 are occupied oxygen ions. After annealing at 700°C with Ca shots in a sealed silica tube, the occupying oxygen ions are replaced by electrons, hence C12A7 becomes an electride. Adopted from [11].

Figure 2.2 Crystal Structure of Ca₂N. Primitive rhombohedral cell and conventional hexagonal cell are indicated as dashed and solid lines, respectively. Adopted from [23].

Figure 2.3 An isosurface of electron density at 0.65×10^3 electrons/nm³. The image is produced by the maximum entropy method combined with Rietveld analysis. Adopted from [19].

Figure 2.4 A microscope image of exfoliated Ca₂N crystal pieces. Green shiny surfaces are pristine Ca₂N surfaces. Dark blue and black surfaces are some reacted surfaces such as CaO and so on.

Figure 2.5 Schematic of the sample preparation procedure.

Figure 2.6 (a) The FS and the first BZ of Ca₂N. (b) The projected FS along the red arrow indicated in (a). Both hexagonal (red solid lines) and rhombohedral (black solid lines) scheme were shown. ARPES probing paths (various k_z values) using 120, 130, and 140 eV were also shown by blue solid lines. Adopted from [23].

Figure 2.7 Experimentally obtained FS map with $h\nu = 120$ eV. FS cuts at certain high symmetry planes (green solid/dashed lines) are shown. Additionally, a constant energy surface on the Γ MK plane at -0.19 eV was shown as red dashed lines. Adopted from [23].

Figure 2.8 ARPES spectra of Ca₂N at (a) $h\nu = 140$ eV and (b) 130 eV. Solid and dashed lines were from DFT calculations. Adopted from [23].

Figure 2.9 Momentum distribution curves of Ca₂N from ARPES spectra shown in the Fig.

2.7. Corresponding used photon energies are (a) $h\nu = 140$ eV and (b) 130 eV. The dashed lines were shifted band dispersions from DFT calculations. Adopted from [23].

Figure 2.10 Orbital characters of the FS-forming band in Ca_2N . Adopted from [23].

Figure 2.11 Summary of the Chapter 2. Adopted from [23].

Figure 3.1 Schematic illustration of the mechanism for generating 2DEG on a BiO₂ terminated surface on BBO. Adopted from [13].

Figure 3.2 Transmission electron microscope images from an interface between SrTiO₃ (STO) and Ba_{0.6}K_{0.4}BiO₃ (BKBO). After 10 seconds of beam exposure, the diffraction patterns were destroyed as shown. BBO also showed a similar result.

Figure 3.3 *in-situ* K dosing process and mechanism to suppress surface intensity.

Figure 3.4 An illustration for schematic introduction for our experiments. (a) Two possibilities on the termination layer, BiO₂- and BaO-termination. (b) Photons and photoelectrons from a film. Note that photoelectrons were generated from different depths, which results in reduction in photoelectron intensity. The reason is that generated photoelectrons have finite escape depths. Adopted from [18].

Figure 3.5 (a) Bi 4*f*_{7/2} core levels and (b) Ba 3*d*_{5/2} core levels from different emission angles. Adopted from [18].

Figure 3.6 Simulated spectral-weight ratios assuming for different situations (black and red solid/dashed lines) and experimental spectral-weight ratio (blue dots). Adopted from [18].

Figure 3.7 Constant energy surfaces below (a) 1.9 eV, (b) 2.3 eV, and (c) 3.0 eV from the Fermi level. Note that the first Brillouin zone (simple cubic zone) and folded zone by crystal structure distortion were indicated as white solid/dashed lines, respectively. Adopted from [18].

Figure 3.8 ARPES spectra along the Γ X Γ Γ line. The high symmetry points were indicated in Fig. 3.7. (a) Normalized spectra by the method describe in the main text. White dashed

line is for a guide. The relative energy level and bandwidth of the top-most valence band were also indicated. (b) Raw ARPES spectra. Adopted from [18].

Figure 3.9 (a) Comparison of ARPES between pristine and K dosed films (b) the same comparison as we did in (a) by clarifying band dispersions using the two-dimensional curvature method described in the main text. The observed difference is disappearance of a flat band located at -3.8 eV marked by a black dashed line. Adopted from [18].

Figure 3.10 Angle-integrated spectra from pristine and K evaporated films. Spectral intensity -3.8 eV is suppressed, which was consistent with the disappearance of the flat band observed in Fig. 3.9. There was no change near the in-gap region even we magnified the spectra 100 times. Adopted from [18]

Figure 4.1 A schematic illustration of the distance between transition metal ions in perovskite oxides. Note that in a well-known ferromagnet BCC Fe the distance between the nearest neighbor is about 0.287 nm.

Figure 4.2 (a) Momentum-resolved band structure of SRO at 100 K. (b) Intensity maxima plots in momentum distribution curves. (c) Temperature-dependent peak positions in momentum distribution curves at $E - E_F = 200$ meV. (d) Energy shift of the annotated peak in (c) Temperature-dependent magnetization curve shape was also displayed for comparison. Adopted from [9].

Figure 4.3 A microscope image of a SRO single crystal on a copper puck for ARPES measurement.

Figure 4.4 A Fermi surface map obtained with various photon energies. We used an energy step of 2 eV. The probing plane in reciprocal space is marked in the right panel. The solid black boundary indicated the simple cubic BZ boundary.

Figure 4.5 Measured FSs on (a) the Γ XM plane and (b) ZRA plane. The BZ boundaries on each map were indicated as black dashed lines. They showed significant difference indicating 3D dispersive nature in the electronic structure of SRO. The measuring regions in the first BZ were shown in the right panels.

Figure 4.6 (a) Band dispersions obtained along the Γ X line and (b) RA line. Notation and specific location of high symmetric points were marked in Fig. 4.5.

Figure 4.7 (a) A FS map on the ZRA plane at $T = 195$ K. (b) Another FS map on the same reciprocal space region at $T = 35$ K. Note that the straight spectral feature now became split into two lines. (c) the same FS map with (b) obtained after *in-situ* K dosing.

Figure 4.8 (a) A FS map on the ZRA plane with LH-polarized radiation and (b) LV-polarized radiation.

Figure 4.9 Experimental geometry of polarization dependent ARPES measurement. Adopted from [20].

Figure 4.10 The split band observed in the FS cut shown in Fig. 4.7 (b). The energy splitting was about 0.1 eV.

Figure 4.11 (a) LDA calculation with and without spin-orbit coupling with ferromagnetic ground state. (b) Overlapped LDA calculation. The experimental spectrum was the same with that in Fig. 4.10.

Figure 4.12 Determining Δ_{ex} in the ARPES spectrum.

Figure 4.13 (a) T vs Δ_{ex} determined by the method described in the main text. A temperature dependent magnetization curve was referred from []. (b) Calculated temperature dependent magnetization and Δ_{ex} (inset). Note that Δ_{ex} did not become zero even above T_{C} . Adopted from [10].

Chapter 1

Introduction

1.1 Free (itinerant) electrons in solids and band structures

Itinerant electrons or free electrons in solids are one of the most important objects in condensed matter physics because they determine key physical properties. Conduction of elemental metals such as alkali metals, alkaline-earth metals, and transition metals had been extensively studied in terms of understanding dynamics of their nearly-free valence electrons [1]. It is recognized that dynamics of itinerant electrons not only in elemental metals in which electron-electron correlation is negligible, but also those in correlated systems are important to understand correlated conduction behavior and ground states. Even the correlated dynamics have attracted noticeable attention because many exotic ground states such as high- T_c superconductivity [2], ferromagnetism [3], heavy Fermion [4], and two-dimensional (2D) electron gases [5] have been realized in bulk or surface states.

Classic theoretical advancements had been established for understanding dynamics of those electrons. The most well-known example is the band theory [1]. The band theory has been essential to study crystalline solids. By using the semiclassical transport theory

(Boltzmann transport) [1], one can determine electrical conducting properties only from band information with a periodic potential. Thus, it should be the priority to have correct band structure information to understand itinerant electron dynamics.

Lots of efforts have been made to understand band structures in both ways; by experiment and by theory. Theoretical understanding on band structure is based on solving many-body Hamiltonian in solids. Since it is impossible to solve the exact many-body Hamiltonian which consider all the electrons in solids, various approximations have been utilized. One of the most famous reducing many-body Hamiltonian to one electron Hamiltonian is density functional theory (DFT). The key idea of density functional theory is adopting electron density functional. To do so, we could reduce many-body interaction part into effective one electron potential which contains two essential interaction part; Coulomb interaction and exchange. How to reduce many-body interaction by introducing an effective one electron potential, an exchange-correlation function, is now the main question for DFT. If correlation between itinerant electrons is negligible, the well-known local density approximation as a choice of exchange-correlation function has *ab-initio* nature and correct solution. However, for correlated systems whose exotic ground states are in the central issues in solid state physics, choosing an appropriate exchange-correlation is demanding. Even correlation allows localized electrons to form Fermi surfaces as depicted in Fig. 1.1. Very recently, so-called beyond-DFT techniques such as dynamic mean field theory (DMFT) has been developed to overcome limitation of DFT [6-7].

In order to have correct band information, it is desired to have complementary band structure information, especially from an experimental way. For the purpose, spectroscopic

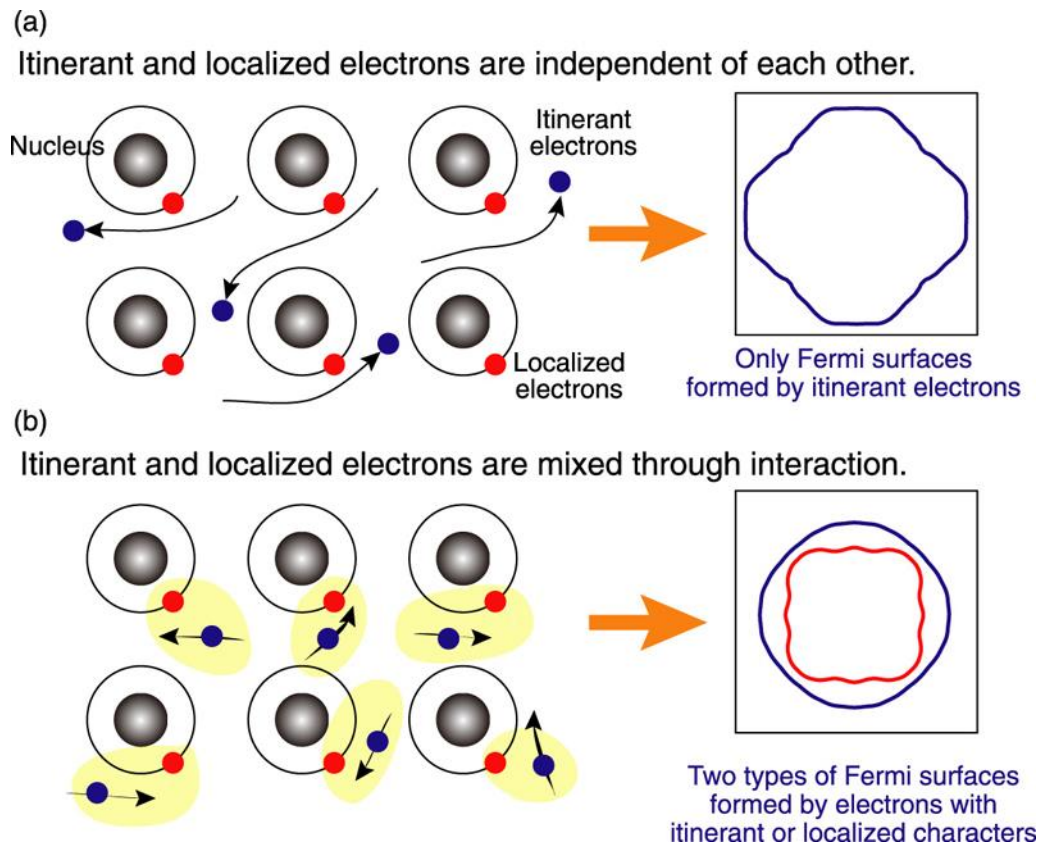


Figure 1.1 Fermi surfaces formed by itinerant and localized electrons. Adopted from [8].

techniques are suitable since their products, various spectra, can be directly compared with theoretical results from DFT and beyond-DFT schemes. One of the most famous spectroscopic techniques to study band structures is photoemission spectroscopy (PES). PES provides one-particle excitation functions which can be easily connected with density of states calculation results. If momenta of photoelectrons can be resolved, PES can even provide momentum-resolved band structure information (a schematic is described in Fig. 1.2). Such experimental information is suitable to be compared with theoretical calculations.

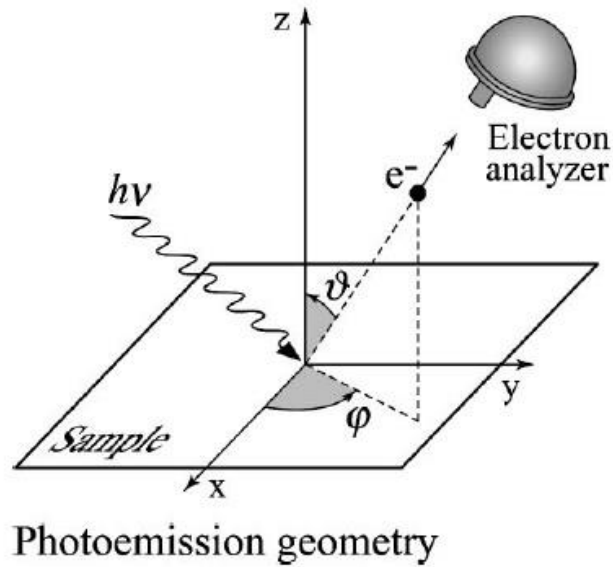


Figure 1.2 A schematic on (angle-resolved) photoemission spectroscopy. Adopted from [8].

Thus, photoemission techniques have been adopted for a long time to study band structures of crystalline solids.

Since determining the correct band structure is more important for correlated systems, there have been a lot of efforts for studying correlated systems in terms of PES. Studying aforementioned exotic ground states – high T_c superconductivity, itinerant ferromagnetism, heavy fermion, and 2D electron gases – by electronic structures are already in central and essential parts of solid state physics researches. Recently, photoemission has not only utilized for studying correlated systems, but also for confirming unexplored physical properties or dimensionality.

Though PES is powerful to study band structures, it is not applicable to all the crystalline

solids. One of the constraints is that a sample needs to be metallic. Since photoemission is on-going during all the measurement, the measured sample needs to be neutralized by excess charges from a charge reservoir. Another disadvantage is that photoemission is very surface sensitive process. A target sample must have very clean surface to well define photoelectron momentum. To maintain clean surfaces, photoemission experiments are almost always conducted in ultrahigh vacuum and cryogenic condition, which acts as a barrier for easy experimental access.

1.2 Photoemission spectroscopy (PES) and angle-resolved photoemission spectroscopy (ARPES)

1.2.1 Basic aspects of photoemission kinematics

PES is an old experimental tool, but still adopted for various purposes and uses and the importance of photoemission experiments has been even becoming significant. When a sample is exposed to photons with energy of $h\nu$ ($h\omega$), it emitted so-called photoelectrons. This is photoelectric effect, which was the first well-known evidence for quantized energy in nature. The maximum kinetic energy of photoelectron is derived from photon energy and a work function of a specific system (Φ) as $E_{\text{kin,max}} = h\nu - \Phi$ [9]. Photoelectrons with smaller kinetic energy are also emitted, thus a systematic energy analysis of photoelectrons showed an energy spectrum. This is a photoemission spectrum, which has relation with density of states of valence band of a system. Obtained valence band information enables us to study

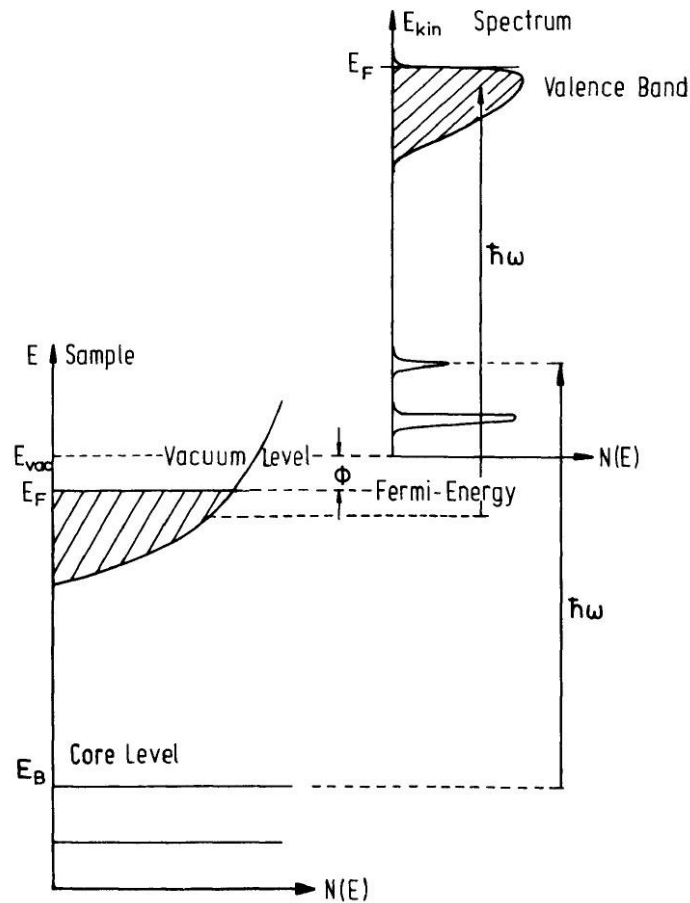


Figure 1.3 A schematic diagram of photoemission energetics. Adopted from [10].

electronic structures. We will discuss PES in detail in this chapter.

A schematic description for energetics of photoemission process was displayed in Fig. 1.3. Obviously, monochromatic radiation ($\hbar\omega$) is needed to produce photoelectrons from surfaces, usually from synchrotron radiation or discharge lamps. After shining up a sample, photoelectrons emit from the sample with momentum p noted as,

$$p = \sqrt{2mE_{kin}} \quad (1.1)$$

As mentioned above, the kinetic energy of photoelectron is determined from photon energy and work functions. Most importantly, binding energies of valence band or core level states inside a solid (E_B) result in an energy spectrum. Considering all, the kinetic energy of photoelectron is determined as

$$E_{kin} = h\nu - \Phi - E_B \quad (1.2)$$

If a sample has well-defined periodicity (i.e. good crystallinity), crystal momentum is a good quantum number for describing electronic structures of the system (Bloch theorem). Since recently developed electron analyzers can obtain emission angles of photoelectrons, we can now infer in-plane crystal momentum by the momentum conservation law. Generally, polar (θ) and azimuthal (φ) angles are determined from an electron analyzer and a sample geometry set by a sample manipulator as shown in Fig. 1.2. Then, the in-plane crystal momentum k_{\parallel} is written as

$$k_{\parallel} = \frac{p_{\parallel}}{\hbar} = \frac{1}{\hbar} \sqrt{2mE_{kin}} \sin\theta \quad (1.3)$$

Note that k_{\parallel} is considered in the extended zone scheme. Consequently, we can detect crystal momentum on the second or higher order Brillouin zone (BZ) with larger θ .

The other component, the out-of-plane component, can be determined with an assumption of nearly-free final bulk Bloch states since the out-of-plane component is not conserved contrary to the case of the in-plane component. With the assumption, we can now write the

out-of-plane component of crystal momentum k_{\perp} as

$$k_{\perp} = \frac{1}{\hbar} \sqrt{2m[E_{kin}(\cos \theta)^2 + V_0]} (\neq \frac{p_{\perp}}{\hbar}) \quad (1.4)$$

from the energy conservation law with photoelectron kinetic energy. Here V_0 is the inner potential, simply given by the sum of work function and valence band bottom energy (E_0).

1.2.2 The three-step model

We described an introductory way to infer crystal momentum and energy in the previous chapter. The photoemission process is, however, more complicated than those simple picture. It is challenging to describe whole photoemission process rigorously since photoelectrons naturally induces many-body effects via Coulomb interaction and so on. Thus, an intuitive understanding of photoemission process has been lacking so far. There have been various tries to intuitively understand the photoemission process, and the three-step model is one of the most well-known description. Here, we shortly describe the key ideas of the *three-step* model.

Optical excitation is necessary to produce photoelectrons, thus the transition probability w_{fi} between initial and final states plays a role. By Fermi's golden rule, w_{fi} is given as

$$w_{fi} = \frac{2\pi}{\hbar} |\langle \psi_f^N | H_{int} | \psi_i^N \rangle|^2 \delta(E_f^N - E_i^N - h\nu) \quad (1.5)$$

Where E_i^N and E_f^N are the initial and final state energies, respectively. The initial and final state energies contain the energy states of initial and final state of $(N-1)$ particles and

one particle initial and final state energy, E_B (binding energy) and E_{kin} (photoelectron kinetic energy), respectively. Concluding them, we can write $E_i^N = E_i^{N-1} - E_B$ and $E_f^N = E_f^{N-1} - E_{kin}$. The interacting Hamiltonian includes optical excitation process, thus it can be obviously written as

$$H_{int} = \frac{e}{2mc} (\vec{A} \cdot \vec{p} + \vec{p} \cdot \vec{A}) = \frac{e}{mc} \vec{A} \cdot \vec{p} \quad (1.6)$$

where \vec{A} and \vec{p} denote the vector potential and the momentum operator, respectively. The second equity is held when $[\vec{p}, \vec{A}] = \frac{\hbar}{i} \vec{\nabla} \cdot \vec{A} = 0$. The commutation becomes zero when spatial distribution of the vector potential is negligible.

We would like to note that in realistic photoemission process many-body effects play an important role, therefore the whole process should be considered as the so-called *one-step* model. The complex behavior is already expected in the Eq. 1.6, since the commutation relation does not become zero when the vector potential disperses. This effect is significant near the sample surface. The treatment of such complicated phenomena can be done within the one-step model. It, however, hardly gives intuitive understanding, thus the three-step model has been widely utilized.

The three-step model includes three independent main steps as a sequence. First of all, there should be an optical excitation process to generate photoelectrons. After the generation, photoelectrons travel to the surface. For the last step, photoelectrons escape from bulk and keep travelling through vacuum. The whole processes should be considered to calculate photoemission intensity. For convenience, we generally consider the first step (optical excitation) to calculate intrinsic photoemission intensity. Others are often treated

as extrinsic effects (This does not mean the second and third steps are not intrinsic characters of photoemission process, but they are aside from inferring the initial many-body wavefunction).

For the initial N -particle state, we may decouple one-particle orbital wavefunction with $(N-1)$ particle wavefunction, assuming the initial N -particle state as a Slater determinant. The initial N -particle state can now be written as

$$\psi_i^N = \phi_i^{\vec{k}} \psi_i^{N-1} \quad (1.7)$$

where $\phi_i^{\vec{k}}$ is one-particle wavefunction. We can also write the final ψ_f^N decoupling the final photoelectron wavefunction from the $(N-1)$ particle wavefunction. Now, the matrix element $\langle \psi_f^N | H_{int} | \psi_i^N \rangle$ in Eq. 1.5 is

$$\langle \psi_f^N | H_{int} | \psi_i^N \rangle = \langle \phi_f^{\vec{k}} | H_{int} | \phi_i^{\vec{k}} \rangle \langle \psi_m^{N-1} | \psi_i^{N-1} \rangle (\propto \langle \phi_f^{\vec{k}} | \vec{A} \cdot \vec{p} | \phi_i^{\vec{k}} \rangle \text{ when } m = i) \quad (1.8)$$

where ψ_m^{N-1} is the m th eigenstate of the final $(N-1)$ particle state. The eigenstate spectrum of the final $(N-1)$ particle states is often considered as the same with that of the initial $(N-1)$ particle states. In this situation, the bracket term $\langle \psi_m^{N-1} | \psi_i^{N-1} \rangle$ in Eq. 1.8 becomes 1 only if m equals to i . Thus, we are able to take the so-called matrix element effect $\langle \phi_f^{\vec{k}} | \vec{A} \cdot \vec{p} | \phi_i^{\vec{k}} \rangle$ into account. The practical example will be presented in Chapter 4.

The three-step model is powerful to understand photoemission process in an intuitive way, and it even provides a way to analyze the matrix element effect in real situations. One should note, however, that the three-step model consists of a lot of assumption which may break down under certain circumstances. We already mentioned that many-body effects

become important. It can be also emphasized when we consider the matrix element effect. The inner product between the initial and final ($N-1$) particle states $\langle \psi_m^{N-1} | \psi_i^{N-1} \rangle$ does not have to be either zero or one. This is because the final ($N-1$) particle can be perturbed by one-electron removal process. In addition, many-body interactions can dress the initial eigenstate spectrum. Such effects become significant when we are studying strongly correlated systems. The details are discussed in some references [11].

1.3 Outline of the thesis

In the thesis, photoemission studies for a 2D electride, Ca_2N and 3D oxide perovskites will be reported. From the studies, we will provide new evidence for exotic ground states which determine conducting nature in the system and an experimental claim for a long-standing controversy. In Chapter 1, roles of itinerant electrons in solids and experimental techniques on photoemission spectroscopy are briefly introduced. Chapter 2 focuses on the electronic structure of an electride Ca_2N . A Fermi surface (FS) map and electronic band dispersion were provided. We picked up a couple of photon energies to study k_z dispersions. The results were consistent with DFT calculations except an unintended chemical potential shift. Therefore, we revealed the quasi-2D nature of the electronic structure of Ca_2N , and existence of the interstitial electrons was strongly supported [12].

In Chapter 3 and 4, we changed the topic to 3D oxide perovskites. The main objective of Chapter 3 is possible surface 2D electron gases on BaBiO_3 . Using the grown BBO films, we obtained angle-resolved valence band spectra. However, the ARPES spectra did not

show any features of metallic states on anywhere in the Brillouin zone. We found that sophisticated theoretical investigations are needed to study the correct electronic structures of BBO [13]. Chapter 4 deals with SrRuO₃, a metallic ferromagnet. We experimentally provided the 3D momentum-resolved electronic structure of SrRuO₃ by ARPES for the first time. By comparing our results with calculations, we showed that the exchange splitting from ferromagnetism did not completely become zero even above the T_C . This is critical experimental evidence for the dual origin in ferromagnetism of SRO.

References

- [1] N. W. Ashcroft, N. D. Mermin, *Solid State Physics* (Brook/Cole, Belmont, 1976)
- [2] J. G. Bednorz and K. A. Müller, *Z. Phys. B* **64**, 189 (1986).
- [3] T. Moriya, Y. Takahashi, *Annu. Rev. Mater. Res.* **14**, 1 (1984).
- [4] G. R. Stewart, *Rev. Mod. Phys.* **56**, 755 (1984).
- [5] S. Stemmer, S. James Allen, *Annu. Rev. Mater. Res.* **44**, 151 (2014).
- [6] Antoine Georges, Gabriel Kotliar, Werner Krauth, Marcelo J. Rozenberg, *Rev. Mod. Phys.* **68**, 13 (1996).
- [7] G. Kotliar, S. Y. Savrasov, K. Haule, V. S. Oudovenko, O. Parcollet, C. A. Marianetti, *Rev. Mod. Phys.* **78**, 865 (2006).
- [8] A. Damascelli, Z. Hussain, and Z.-X. Shen, *Rev. Mod. Phys.* **75**, 473 (2003).
- [9] A. Einstein, *Ann. Physik* **17**, 132 (1905).
- [9] M. Cardona and L. Ley, *Photoemission in Solids I: General Principles* (Springer-Verlag Berlin Heidelberg, 1978).
- [10] S. Hüfner, *Photoelectron Spectroscopy* (Springer-Verlag Berlin Heidelberg, 2003).
- [11] L. Hedin, *J. Phys. Condens. Matter* **11**, R489 (1999).
- [12] J. S. Oh, C.-J. Kang, Y. J. Kim, S. Sinn, M. Han, Y. J. Chang, B.-G. Park, S. W. Kim, B. I. Min, H.-D. Kim, T. W. Noh, *J. Am. Chem. Soc.* **138**, 2496 (2016).
- [13] J. S. Oh, M. Kim, G. Kim, H. G. Lee, H. K. Yoo, S. Sinn, Y. J. Chang, M. Han, C. Jozwiak, A. Bostwick, E. Rotenberg, H.-D. Kim, T. W. Noh, *Curr. Appl. Phys.* **18**, 658 (2018).

Chapter 2

Direct Evidence for 2D Anionic Excess Electrons in an Electride Ca₂N

2.1 Introduction

“X-ide” stands for an ionic crystal with anion X . In this sense, “Electrides” are exotic materials, where electrons themselves play a role as anions. Their unique physical and chemical properties triggered a lot of attentions [1-3]. The exotic properties come from excess electrons, which are apparently highly reactive. In spite of such reactivity, a thermally and chemically stable electride $[\text{Ca}_{24}\text{Al}_{28}\text{O}_{64}]^{4+}(4e^-)$ (C12A7) was synthesized by a Japanese group [4]. As expected, it showed promising functionality. For examples, its applications have been developed for field emission devices and ammonia synthesis [5-6]. Anionic excess electrons in C12A7 are captured in zero-dimensional cavities (shown in Fig. 2.1), and the cavities distributes as a three-dimensional (3D) system. Thus, its temperature-dependent conductivity follows 3D variable range hopping behavior [4]. Including C12A7, many electrides showed localized or delocalized conduction behavior (even superconductivity) followed by their networks of confining sites [7-10].

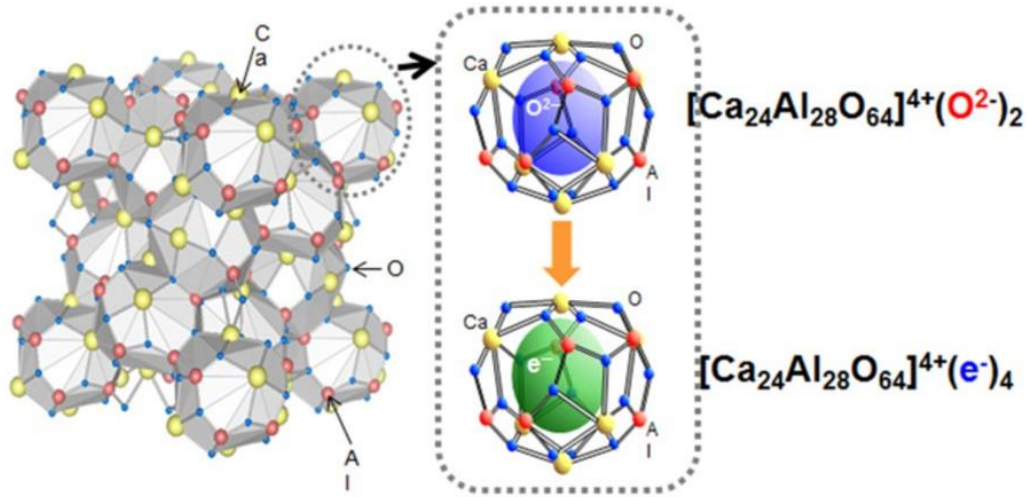


Figure 2.1 Crystal Structure of C12A7. Initially cavities in C12A7 are occupied oxygen ions. After annealing at 700°C with Ca shots in a sealed silica tube, the occupying oxygen ions are replaced by electrons, hence C12A7 becomes an electride. Adopted from [11].

Recently, Lee *et al.* successfully synthesized a single-crystalline Ca_2N which has two-dimensional (2D) crystal structure [12]. Nominal valences of each atom in Ca_2N is Ca^{2+} and N^- , hence it can be written as $[\text{Ca}_2\text{N}]^+e^-$. Figure 2.2 showed the crystal structure of Ca_2N . Ca_2N consists of slabs stacked in the order of Ca-N-Ca. The interlayer spacing between nearest slabs is 3.86 Å. Note that the bond length between Ca and N is 2.44 Å. The large interlayer spacing decouples and electrostatically stabilize electric potential in the interlayer region, thus excess electrons are expected to stay in the region [13].

Density functional theory (DFT) calculations are adopted to probe that excess electrons. The expected location of those electrons were indicated as blue strokes in Fig. 2.2. Following the calculation results, excess electrons, as known as *interstitial electrons*, two-

(3) Ions occupying outmost layer of each slab should be cations to stabilize electrostatic potential in the interlayer region. (4) Sum of oxidation numbers should be positive. Ca_2N satisfies those screening conditions, and its variation Sr_2N , Ba_2N also do. In addition, some carbides were predicted to have quasi-2D interstitial electrons. One of the candidates, Y_2C , was realized very recently by Park *et al* [18]. Even though other candidates have not been synthesized as single crystals so far, interests on 2D electrides keep growing among physicists, chemists, and material scientists.

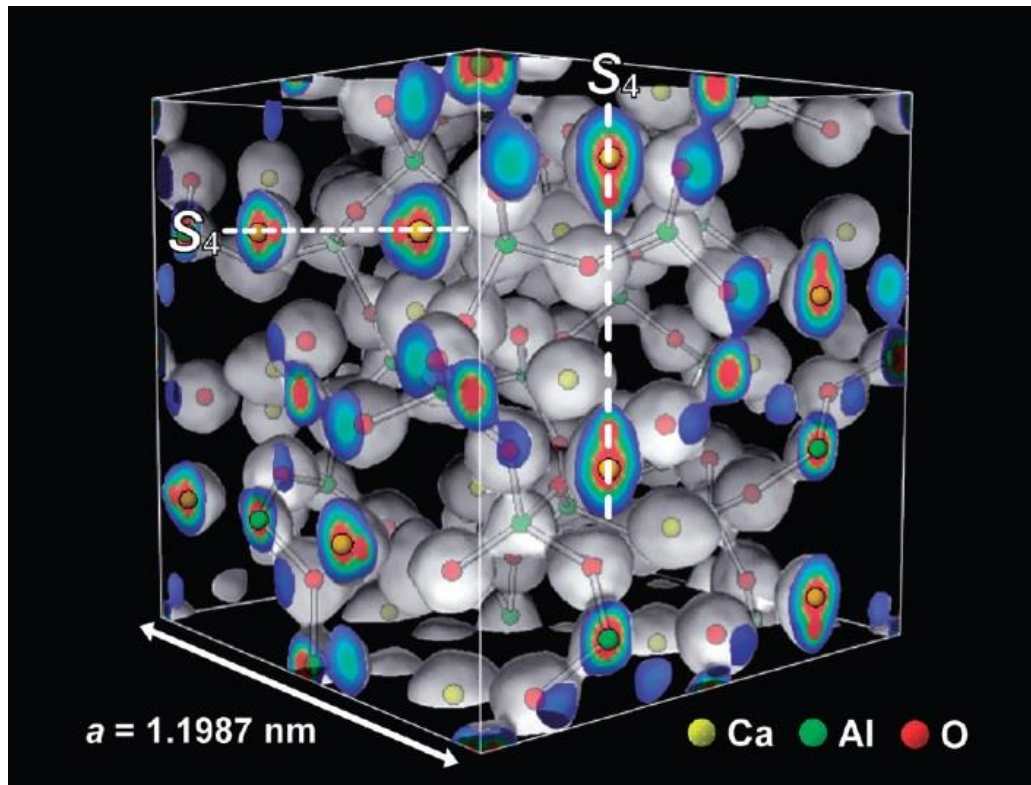


Figure 2.3 An isosurface of electron density at $0.65 \times 10^3 \text{ electrons/nm}^3$. The image is produced by the maximum entropy method combined with Rietveld analysis. Adopted from [19].

Despite extensive investigations on electrides (not just on 2D electrides), promising and convincing evidence for the anionic excess electrons has not been much provided. Among various experimental approaches, x-ray scattering may map charge-density in an electride and can be compared with the Rietveld analysis combined with the maximum entropy method. The combined investigation was performed for C12A7 [19], and off-centered distribution of excess electrons in cavities was revealed as shown in Fig. 2.3. Unfortunately, the charge-density mapping using x-ray scattering for 2D electrides is unlikely at this moment due to low density of interstitial electrons. Only plausible results have been produced from their alkalide counterparts [20-22]. As mentioned above, DFT calculations for 2D electrides have been utilized to investigate their electronic structures. It was theoretically shown that the excess electrons are located in the interlayer region. However, there has been no experimental report to confirm the predictions made by DFT calculations. Moreover, even a simple measurement for these electrides is difficult since many electrides are chemically reactive.

To overcome the limitation of experimental supports for the existence of quasi-2D excess electrons and difficulties with handling Ca_2N , conducting angle-resolved photoemission spectroscopy (ARPES) under an ultra-high vacuum (UHV) and at a cryogenic temperature. ARPES is especially useful for our purpose since it can directly give band structure information which can be compared with DFT calculation results. An UHV and cryogenic environment are also useful to suppress chemical reactivity of Ca_2N . Under such advantages, by obtaining electronic structure information, we can have a smoking gun to confirm DFT calculation results. Finally, we can provide critical evidence for the existence

of the quasi-2D excess electrons.

Here, we investigated the electronic structure of Ca_2N . A Fermi surface (FS) map and electronic band dispersion were provided. We picked up a couple of photon energies to study k_z dispersions. The results were consistent with DFT calculations except an unintended chemical potential shift. Therefore, we revealed the quasi-2D nature of the electronic structure of Ca_2N , and existence of the interstitial electrons was strongly supported [23].

2.2 Methods

Single-crystalline Ca_2N samples were synthesized by the reported recipe [12]. As described in the introduction part, Ca_2N is chemically reactive under air. Hence, we used a glove box filled with 99.999 % Ar gas to prepare samples for ARPES measurements. Figure 2.4 showed typical exfoliated surfaces of Ca_2N . Successfully exfoliated or cleaved surfaces show green shiny surfaces. Note that there were dark blue or black surfaces in Fig. 2.4. The dark blue or black surfaces were consequence from unintended chemical reaction with the environment. The results are calcium oxides or nitrides. The microscope image itself showed how necessary delicate sample preparation is.

Sample preparation process was described in Fig. 2.5. We attached the crystals using silver epoxy on aluminum ARPES sample holders. The attached samples were azimuthally

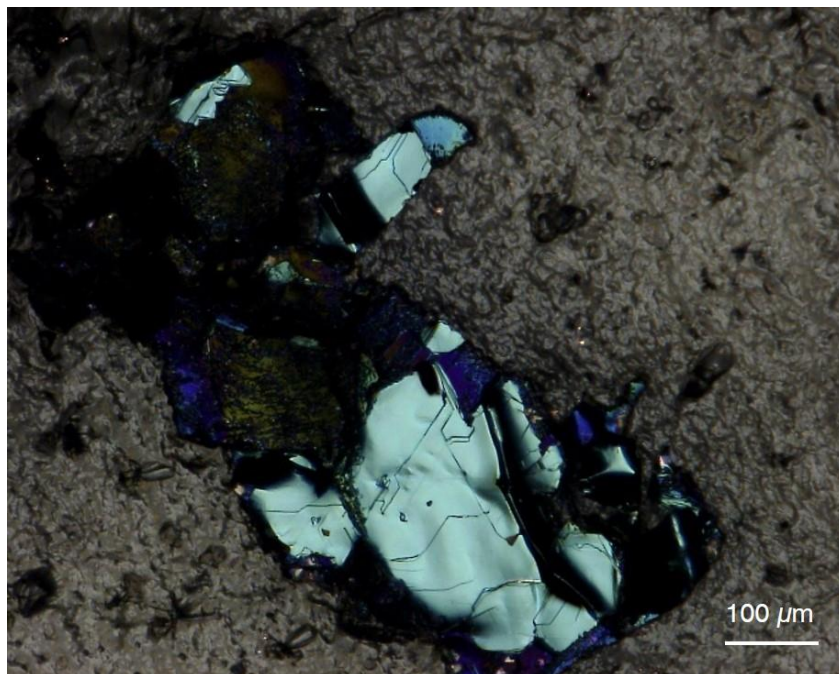


Figure 2.4 A microscope image of exfoliated Ca₂N crystal pieces. Green shiny surfaces are pristine Ca₂N surfaces. Dark blue and black surfaces are some reacted surfaces such as CaO and so on.

aligned within 2 degrees by eyes. For *in-situ* cleaving, we put alumina posts on the top of the attached crystals. As a special development for Ca₂N, we applied UHV grease (Apiezon N grease, Apiezon) to the uncovered side of the samples. The early part of sample preparation was conducted in the home-lab glovebox, and putting alumina posts was processed afterward in a glove bag (Sigma-Aldrich). After preparing the samples, we put the samples into a load-lock chamber as quickly as possible, and now they can be free from air contact.

We conducted APRES measurements at the 4A1 beamline of PLS-II with a Scienta R4000

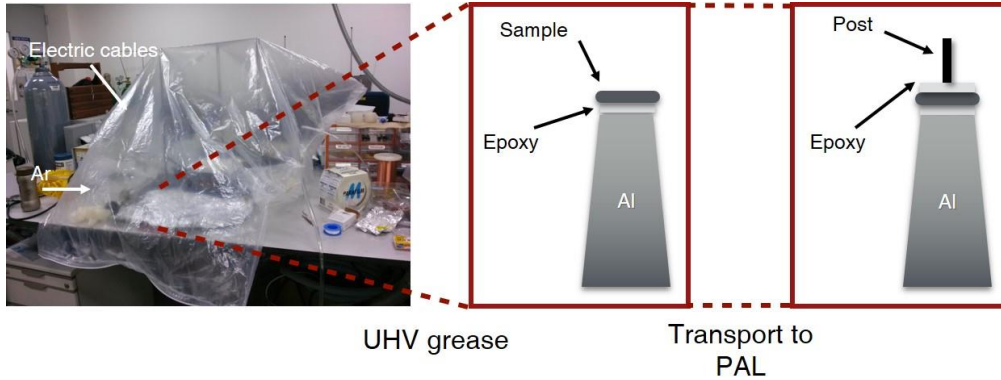


Figure 2.5 Schematic of the sample preparation procedure.

electron analyzer. The inserted samples were cleaved right before performing ARPES experiments. To prevent the cleaved surfaces, the base pressure of the ARPES analysis chamber kept below 2×10^{-11} Torr. All the measurements were performed at 100 K. We obtained 120, 130, and 140 eV of photon energies. Total energy resolution was about 50 meV.

The electronic structure calculations were performed by using the full-potential linearized augmented plane-wave band method, as implemented in the WIEN2K package [24]. The crystal structure was adopted from the experimental structure [12]. For the exchange–correlation, we have utilized the generalized gradient approximation (GGA) of Perdew, Burke, and Ernzerhof. The Brillouin zone integration was done with a $36 \times 36 \times 36$ k -mesh, and muffin-tin radii R_{MT} of Ca and N were chosen to be 2.35 and 2.24 a.u., respectively, and the plane-wave cutoff was $R_{\text{MT}}K_{\text{max}} = 7$. The maximum L value for the waves inside the atomic spheres, $L_{\text{max}} = 10$, and the largest G in the charge Fourier expansion $G_{\text{max}} = 12$ were used in the calculations.

2.3 Result and discussion

2.3.1 Fermi surface of Ca_2N

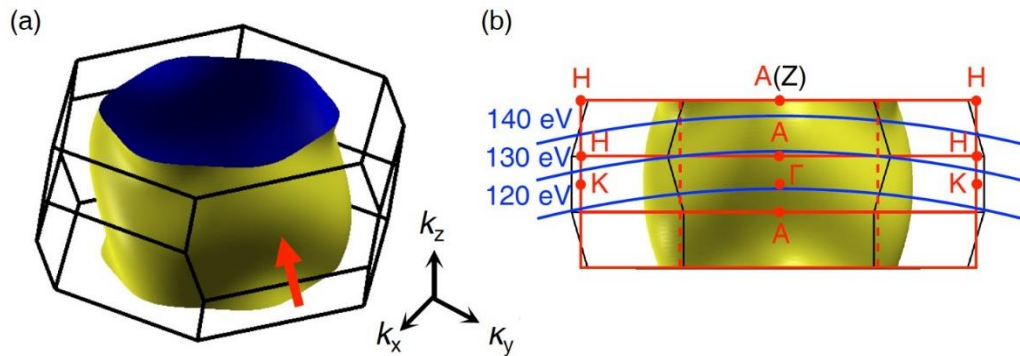


Figure 2.6 (a) The FS and the first BZ of Ca_2N . (b) The projected FS along the red arrow indicated in (a). Both hexagonal (red solid lines) and rhombohedral (black solid lines) scheme were shown. ARPES probing paths (various k_z values) using 120, 130, and 140 eV were also shown by blue solid lines. Adopted from [23].

Fermi surface (FS) topology is one of the most important key to understand dimensionality of a metallic system. As shown in the crystal structure (Fig. 2.2), Ca_2N has a rhombohedral structure. We here used the hexagonal unit cell scheme for convention. Figure 2.6 (a) showed the 3D FS overview in the first Brillouin zone (BZ) from DFT calculations. Black solid line boundary indicated the first BZ in the rhombohedral zone scheme (primitive cell). The 3D FS overview in the primitive zone scheme is complex to understand, thus we projected the 3D FS along the red arrow as indicated in Fig. 2.6 (b). The red solid boundary

in Fig. 2.6 (b) formed a slab-shaped BZ boundary. This is a consequence of the hexagonal cell convention. The zone length of the hexagonal cell along the z -axis is one third that of the rhombohedral cell. The yellow nearly cylindrical object in Fig. 2.6 (b) is the FS. Its shape is a warped open cylinder along the z -axis. Predicted shape of FS is helpful to understand the quasi-2D nature of the electronic structure of Ca_2N . Note that Ca_2N possesses the interstitial electrons in the layered structure.

In ARPES measurement, as noted in the Chapter 1, photons with different energies probe different k -space paths. Therefore, we should adopt various photon energies to cover the whole First BZ. Unfortunately, Ca_2N single crystals are too sensitive to the environment even in the UHV condition. This was the crucial reason why we could not map the whole first BZ using finely tuned photon energies. Despite such disadvantage, we developed a quick procedure to obtain ARPES spectra at a chosen photon energy. We found that the inner potential $V_0 = 16.6$ eV which is roughly the sum of binding energy of N $2s$ (12.3 eV) and the work function of the electron analyzer (4.3 eV).

We experimentally mapped the FS of Ca_2N . The obtained FS using $h\nu = 120$ eV was shown in Fig. 2.7. The map has an energy window of 50 meV centered at the Fermi level. The map was normalized by the maximum and minimum values along each row and column. Although the data quality was not of high quality as conventional ARPES data, we could clearly distinguish FS features from the background. The shape of the experimentally obtained FS was nearly cylindrical as inferred theoretically in Fig. 2.6. We overlaid FS cuts on the ΓMK and ALH high symmetry planes from the DFT calculations by green solid and dashed lines, respectively.

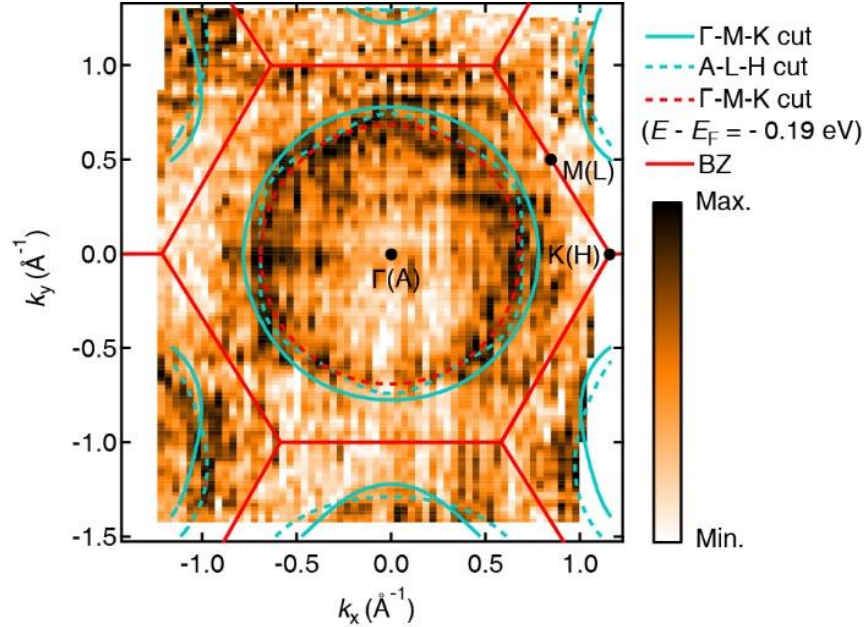


Figure 2.7 Experimentally obtained FS map with $h\nu = 120$ eV. FS cuts at certain high symmetry planes (green solid/dashed lines) are shown. Additionally, a constant energy surface on the Γ MK plane at -0.19 eV was shown as red dashed lines. Adopted from [23].

Both calculated cuts agreed well in terms of its shape. However, the size of the experimental FS was little smaller than the DFT cuts. We suspected that this discrepancy might come from chemical potential shift due to electron depletion on a cleaved surface. Since the loosely bound electrons in Ca_2N will be exposed to residual gas such as H_2O or CO after cleavage as demonstrated in the glove box (see Fig. 2.4). Contacts between cleaved surfaces and residual gases results in insulating contaminants on the surface. Thus, electrons became depleted near the surface which induces a downward chemical potential shift. A significant amount of charge transfer from excess electrons in a Ca_2N monolayer

to certain adsorbates has been demonstrated [25], which justifies our suspicion.

To match the size of FS, we shifted the DFT band dispersions upward by 0.19 eV. By the shift, the size of theoretically calculated FS became smaller hence the agreement can be found. Overall agreement had been way better after shifting the chemical potential, but there was still a small mismatch in their exact shapes. The last-standing mismatch was probably due to the difference in probing path of ARPES as shown in Fig. 2.6 (b).

2.3.2 Band dispersions of Ca_2N

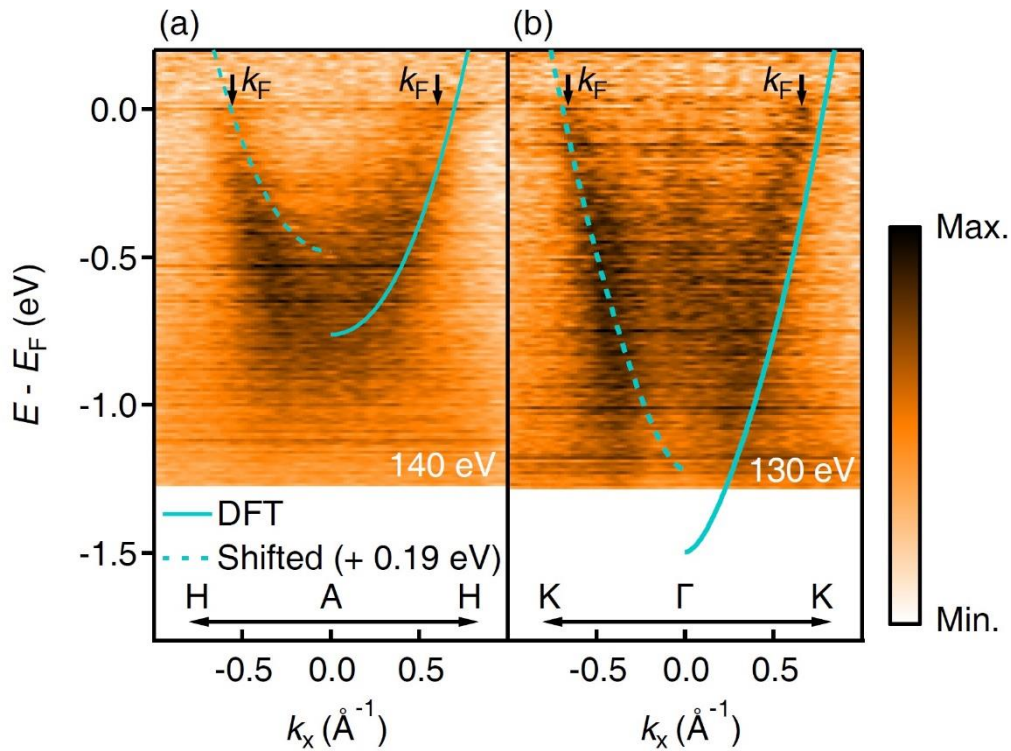


Figure 2.8 ARPES spectra of Ca_2N at (a) $h\nu = 140$ eV and (b) 130 eV. Solid and dashed lines were from DFT calculations. Adopted from [23].

We examined the band dispersions of Ca_2N . We obtained the dispersions using $h\nu = 130$ and 140 eV on the ΓKHA plane. Figure 2.8 showed the results after the normalization method used to enhance the quality of Fig. 2.7. Both experimental spectra showed similar Fermi momenta (k_F) as denoted in Fig. 2.8 (a) and (b). However, their band minima were deviating. The minima at $h\nu = 140$ eV was -0.7 eV while that at $h\nu = 130$ eV was about -1.3 eV. This notable difference indicated there is 3D dispersive features in electronic structures which was not observed by simple analysis on k_F . This dispersive nature was actually already predicted by DFT calculations [12].

Comparison ARPES spectra with DFT calculations could give further insights. We first looked on the dispersion obtained using $h\nu = 140$ eV. Note that the band minimum was similar to that on the high symmetric point A(Z) (see Fig. 2.6 (b)). Thus we compared it with DFT calculations results on the A-H line. We overlapped the DFT results on the experimental spectra by green solid lines. It is obvious that k_F values obtained from the experimental spectra and DFT did not match with each other. This was due to the electron depletion mention in the previous subchapter. Following the analysis method for taking the depletion into account, we shifted the DFT results by 0.19 eV. As we observed in the FS comparison, the critical disagreement was resolved. The k_F values matched well with each other. There was still minor discrepancy on high binding energy side, which could be due

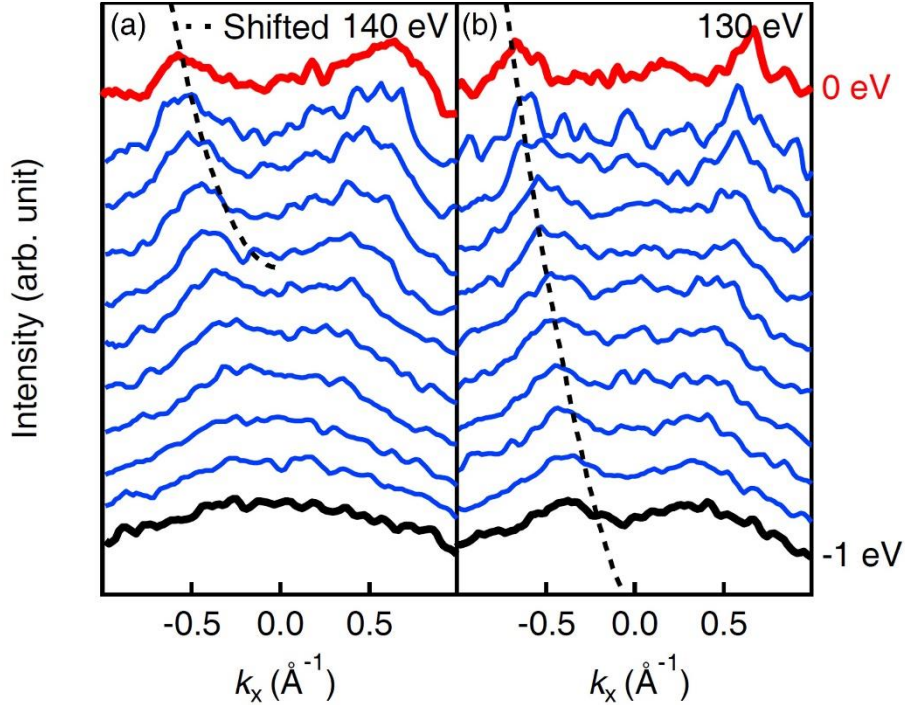


Figure 2.9 Momentum distribution curves of Ca_2N from ARPES spectra shown in the Fig. 2.7. Corresponding used photon energies are (a) $h\nu = 140$ eV and (b) 130 eV. The dashed lines were shifted band dispersions from DFT calculations. Adopted from [23].

to the difference in the ARPES probing path (also discussed in the previous chapter).

An analogous comparison was also performed for the ARPES spectra obtained from $h\nu = 130$ eV. We employed the DFT dispersion along the Γ -K line since the k_z dispersive nature up to the middle point of Γ -A line was not significant [12]. The overall dispersion shape was more dispersive than the dispersion obtained using $h\nu = 140$ eV. The DFT results were also shifted for the same reason mentioned above, and the experimental and theoretical k_F values showed a good agreement. To clarify the comparison, we plotted momentum

distribution curves of the ARPES spectra using $h\nu = 130$ and 140 eV in Fig. 2.9. Figure 2.9 (a) and (b) showed momentum distribution curves from -1.0 eV to the Fermi level by integrating with an energy window of 50 meV. The shifted band dispersions from DFT calculations were also overlaid. Additional to the good agreement we found from the ARPES intensity maps and overlapped band dispersions, momentum distribution curves also showed there were spectral signatures on where the DFT results predicted.

2.3.3 Orbital characters of the valence band

The comparison made in two previous chapters showed that the DFT calculations and experimental results agreed well. However, a puzzle still remained, which is the origin of 3D dispersive nature in our ARPES spectra. As demonstrated, they had notable k_z dependence and were even quiet dispersive. The signatures were easily found the difference of the band minima in ARPES spectra obtained from $h\nu = 130$ eV and 140 eV. In addition, DFT calculations from Lee *et al.* (or ours) showed the k_z -dispersive nature. Considering that the excess electrons play a role as anions in the interstitial region, they can bridge or form a weak bonding between Ca_2N slabs. Hence, the electronic structure of Ca_2N naturally becomes 3D in contrast to nearly-constant k_F values along the k_z direction and the observed quasi-2D cylindrical FS.

The answer to the puzzle may be suggested by analyzing the orbital characters of the valence band which mainly contributes to the quasi-2D FS. Figure 2.10 showed the orbital characters of the valence bands, derived from the DFT calculations. Generally orbital

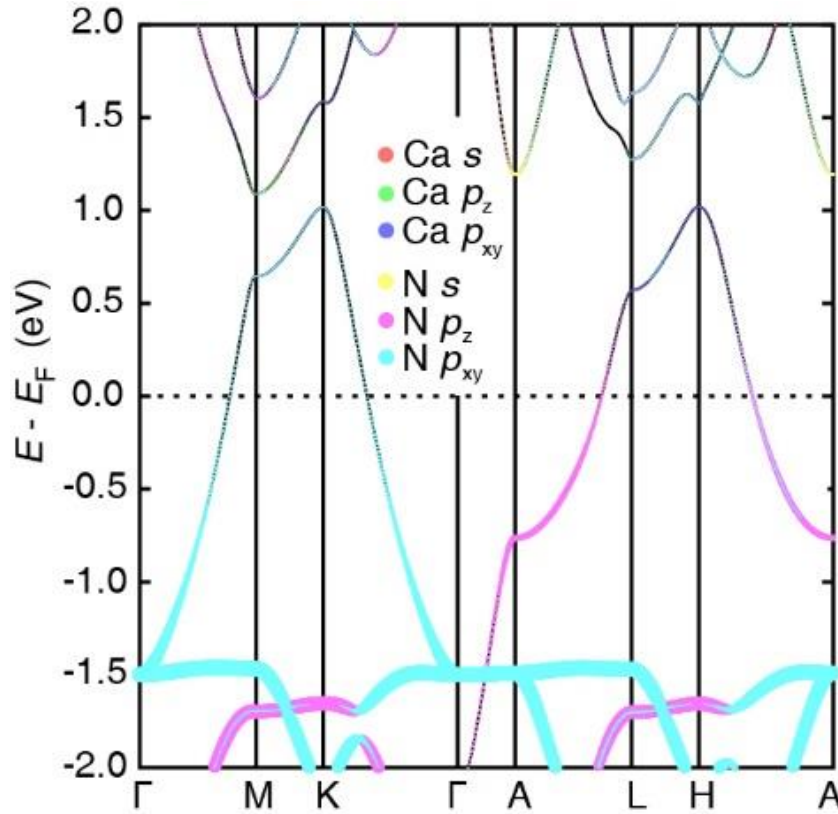


Figure 2.10 Orbital characters of the FS-forming band in Ca_2N . Adopted from [23].

characters are calculated by computing an inner product of atomic Wannier functions and an eigenstate. Since the bases of interstitial electrons are not atomic orbitals, we could not calculate the orbital characters of the interstitial electrons.

The key idea found in the orbital character calculations is the difference between orbital characters of the valence band on the ΓMK plane and the ALH plane. On the ΓMK plane, in-plane orbitals such as $\text{N } 2p_{xy}$ dominates the valence band. Contrary to this case, out-of-plane orbitals like $\text{N } 2p_z$ contributes the valence band on the ALH plane. Other orbitals ($\text{Ca } 4s$, $3p$ and $\text{N } 2s$) were located too far from the Fermi level, thus hardly contributed low-energy excitation or conduction in Ca_2N .

Now we may understand the overall electronic structure of Ca_2N as follows. On the ΓMK plane ($k_z = 0$), the valence band should be more dispersive than that on the ALH plane since in-plane orbitals are main contributors. As our observing k_z value increases, the valence band quickly approaches the Fermi level, considering the initial nearly-free electron nature (without considering the dimensionality). Even though the nearly-free electronic dispersion rapidly approaches to the Fermi level, it still lies below the Fermi level. This is because of the long c -axis in the layered crystal structure. The long c -axis lattice parameter reduces one k_z period in reciprocal space. Thus, the electronic dispersion cannot disturb the feature near the Fermi level. The in-plane dispersion became suppressed on the ALH plane since out-of-plane orbitals now governs the valence band. Consequently, in-plane dispersion is suppressed and k_F values on the ΓMK and the ALH plane can remain the similar value.

2.4 Conclusion

Taking our suspicion on the chemical potential shift, we found that there were reasonably good agreements between experimental spectra and DFT results in the FS and band dispersions. The good agreements showed that other predictions from DFT calculated results can be considered as reliable ones. For instance, the electron density maps suggested by Lee et al. now becomes a powerful support for the existence of the interstitial electrons. If there were no interstitial electrons, hybridizations between electrons on the outmost layers on each slab occur, and FS topology would dramatically change as a result. However, this did not happen in reality as demonstrated by our ARPES experiments.

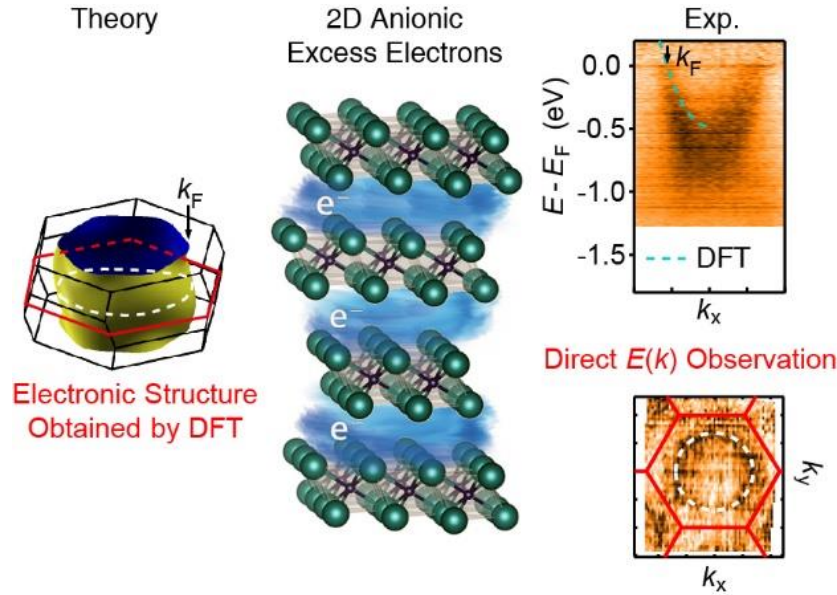


Figure 2.11 Summary of the Chapter 2. Adopted from [23].

Note that the electron density of the interstitial electrons is too low to be detected by any x-ray scattering techniques. Though there were certain difficulties that we should overcome, ARPES provided plausible evidence for the existence of interstitial electrons by directly probing DFT calculations. Additionally, the good agreement between ARPES and DFT calculations demonstrated that electron-electron correlations are not significant in Ca_2N , which guides further theoretical or spectroscopic studies on Ca_2N .

In summary, we investigated the electronic structure of an electride Ca_2N by ARPES. Using various photon energies, we could determine k_z dispersion in the electronic structure, whereas the k_F values nearly remain as a constant. Hence, we confirmed that low-energy excitation or conduction governed by the electronic structure very near the Fermi level should be quasi-2D. Good agreements between ARPES and DFT results showed that all the consequent results from DFT calculations can be reliable if it successfully reproduces

the electronic structure. Thus, we provided firm evidence for the existence of the anionic excess electrons in the interstitial region in Ca_2N .

References

- [1] J. L. Dye, *Science* **247**, 663 (1990).
- [2] J. L. Dye, *Inorg. Chem.* **36**, 3816 (1997).
- [3] J. L. Dye, *Acc. Chem. Res.* **42**, 1564 (2009).
- [4] S. Matsuishi, Y. Toda, M. Miyakawa, K. Hayashi, T. Kamiya, M. Hirano, I. Tanaka, H. Hosono, *Science* **301**, 626 (2004).
- [5] Y. Toda, S. Matsuishi, K. Hayashi, K. Ueda, K. Kamiya, M. Hirano, H. Hosono, *Adv. Mater.* **16**, 685 (2004).
- [6] M. Kitano, Y. Inoue, Y. Yamazaki, F. Hayashi, S. Kanbara, S. Matsuishi, T. Yokoyama, S. W. Kim, M. Hara, H. Hosono, *Nat. Chem.* **4**, 934 (2012).
- [7] J. E. Medvedeva, A. Freeman, *Appl. Phys. Lett.* **85**, 955 (2004).
- [8] P. V. Sushko, A. L. Shluger, M. Hirano, H. Hosono, *J. Am. Chem. Soc.* **129**, 942 (2007).
- [9] S. W. Kim, S. Matsuishi, T. Nomura, Y. Kubota, M. Takata, K. Hayashi, T. Kamiya, M. Hirano, H. Hosono, *Nano Lett.* **7**, 1138 (2007).
- [10] M. Miyakawa, S. W. Kim, M. Hirano, Y. Kohama, H. Kawaji, T. Atake, H. Ikegami, K. Kono, H. Hosono, *J. Am. Chem. Soc.* **129**, 7270 (2007).
- [11] H. Hosono, K. Tanabe, E. Takayama-Muromachi, H. Kageyama, S. Yamanaka, H. Kumakura, M. Nohara, H. Hiramatsu, S. Fujitsu, *Sci. Technol. Adv. Mater.* **16**, 033503 (2015).
- [12] K. Lee, S. W. Kim, Y. Tada, S. Matsuishi, H. Hosono, *Nature* **494**, 336 (2013).

- [13] T. Inoshita, S. Jeong, N. Hamada, H. Hosono, *Phys. Rev. X* **4**, 031023 (2014).
- [14] T. Tada, S. Takemoto, S. Matsuishi, H. Hosono, *Inorg. Chem.* **53**, 10347 (2014).
- [15] X. Zhang, Z. Xiao, L. Hechangm Y. Toda, S. Matsuishi, T. Kamiya, S. Ueda, H. Hosono, *Chem. Mater.* **26**, 6638 (2014).
- [16] S. Guan, S. A. Yang, L. Zhu, J. Hu, Y. Yao, *Sci. Rep.* **5**, 12285 (2015).
- [17] W. Ming, M. Yoon, M.-H. Du, K. Lee, S. W. Kim, *J. Am. Chem. Soc.* **138**, 15336 (2016).
- [18] J. Park, K. Lee, S. Y. Lee, C. N. Nandadasa, S. Kim, K. H. Lee, Y. H. Lee, H. Hosono, S.-G. Kim, S. W. Kim, *J. Am. Chem. Soc.* **139**, 615 (2017).
- [19] T. Nomura, K. Hayashi, Y. Kubota, T. Kamiya, M. Hirano, M. Takata, H. Hosono, *Chem. Lett.* **36**, 902 (2007).
- [20] A. S. Ellaboudy, C. J. Bender, J. Kim, D. H. Shin, M. E. Kuohenmeister, G. T. Baboook, J. L. Dye, *J. Am. Chem. Soc.* **113**, 2347 (1991).
- [21] J. McCracken, D. H. Shin, J. L. Dye, *Appl. Magn. Reson.* **3**, 305 (1992).
- [22] M. E. Kuchenmeister, J. L. Dye, *J. Am. Chem. Soc.* **111**, 935 (1989).
- [23] J. S. Oh, C.-J. Kang, Y. J. Kim, S. Sinn, M. Han, Y. J. Chang, B.-G. Park, S. W. Kim, B. I. Min, H.-D. Kim, T. W. Noh, *J. Am. Chem. Soc.* **138**, 2496 (2016).
- [24] P. Blaha, K. Schwarz, G. K. H. Madsen, D. Kvasnicka, and J. Luitz, *WIEN2k*, (Karlheinz, Schwarz, Techn. Universitat Wien, Austria, 2001).
- [25] S. Zhao, Z. Li, J. Yang, *J. Am. Chem. Soc.* **136**, 13313 (2014).

Chapter 3

Absence of Metallic Surface States in BiO₂-Terminated BaBiO₃ Thin Films

3.1 Introduction

Two-dimensional electron gases (2DEGs) at surfaces or interfaces of semiconductors or insulators have been attracting much attention for device applications due to their superior physical properties [1]. They usually possess high electron mobility and conductivity, which enables various ways to adopt for components of electronic devices. 2DEGs was originally realized in an interface between semiconductors, and now they have been produced in oxide heterostructures [2-4]. The so-called oxide 2DEGs showed exotic physical properties such as superconductivity [5] and ferromagnetism [6]. The unique physical properties and ground states of oxides 2DEGs triggered a lot of attentions [7-8].

A perovskite oxide with non-transition-metal BaBiO₃ (BBO) has semiconducting ground state with charge-density-wave (CDW) instability [9-11]. The semiconducting nature has been in a debate, since the appearing semiconducting nature is not intuitive to understand. Assume that all the ions in BBO have their nominal valences. Then, Ba, Bi, and O ions should have the valences of 2+, 4+, and 2-, respectively. Considering the electronic

configuration of Bi^{4+} which is a half-filling of the 6s orbital ($6s^1$), one expects that BBO shows metallic properties. As mentioned above, BBO does not, however, show metallic properties but the semiconducting nature with an optical gap of 2.0 eV. The 2.0 eV optical gap was assigned as a charge-density-wave originated peak [9]. This has been most counter-intuitive, thus early theoretical and experimental approaches to BBO had focused on tracing the origin of the semiconducting nature.

To explain the semiconducting nature of BBO, a charge disproportionation picture has been proposed. The charge disproportionation considers that two nearest Bi ions have 3+ and 5+ of valences rather than 4+. The unstable $6s^1$ electronic configuration of a Bi ion supported the charge disproportionation picture. By some early report, the charge disproportionation picture was supported by observing Bi core levels [12].

A recent theoretical suggestion of existence of a surface 2DEG of BBO was made based on the charge disproportionation scenario by Vildosola, Güller, and Llois (VGL) [13]. The suggestion based on DFT calculations predicted that the surface 2DEG can be generated on a BiO_2 -terminated BBO (001) surface (note that a termination layer of perovskite ABO_3 (001) can be either AO or BO_2). The proposed mechanism is the so-called self-doping effect, as illustrated in Fig. 3.1. If the surface were terminated with a BiO_2 layer, the top-most layer has a missing neighboring oxygen. The neighboring oxygens are taking (giving) charges from (to) Bi^{5+} (Bi^{3+}) ions, thus the charge disproportionation can sustain. The incomplete octahedral environment at the top-most layer results in suppression of charge disproportionation. Then, the excess (deficient) charge will redistribute on the surface, and surface 2DEG can be generated. Note that the proposed mechanism by VGL is different

from existing mechanism such as band bending [14], polar catastrophe [2], and oxygen vacancies [15]. This proposed mechanism had attracted attention since it is not only applicable to BBO, but all other charge-skipping oxide perovskite which are CaFeO_3 [16] and LuNiO_3 [17].

The experimental approaches to BBO, however, are difficult. Contrary to layered compounds, flat surfaces by conventional cleaving for perovskites are hardly producible due their three-dimensional crystal structures. This probably has been one of the most critical difficulties, since angle-resolved photoemission spectroscopy (ARPES), which is a direct way to observe surface 2DEGs, need a flat surface to well determine electron

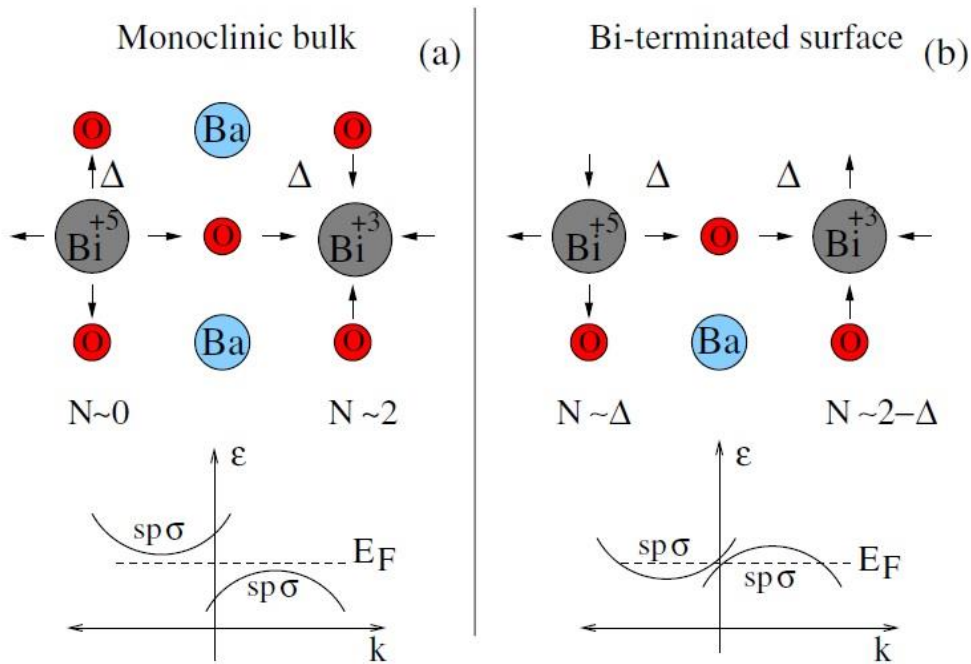


Figure 3.1 Schematic illustration of the mechanism for generating 2DEG on a BiO_2 terminated surface on BBO. Adopted from [13].

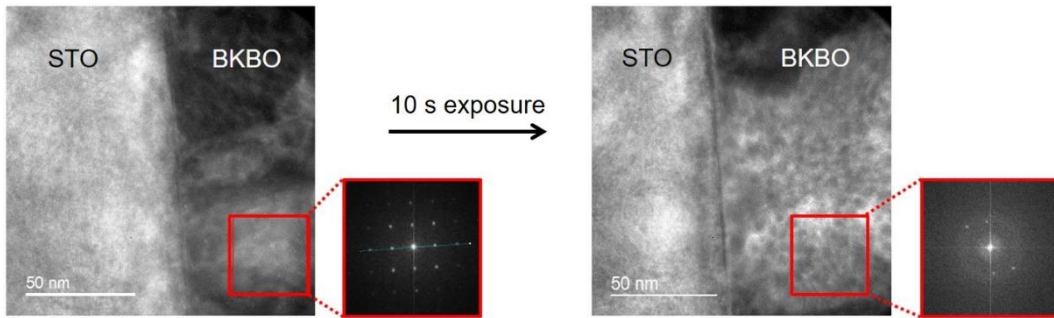


Figure 3.2 Transmission electron microscope images from an interface between SrTiO₃ (STO) and Ba_{0.6}K_{0.4}BiO₃ (BKBO). After 10 seconds of beam exposure, the diffraction patterns were destroyed as shown. BBO also showed a similar result.

momentum. In addition, visualizing and determining the termination layer were also not easy. Figure 3.2 showed diffraction patterns from transmission electron microscope images from SrTiO₃ (noted as STO) and Ba_{0.6}K_{0.4}BiO₃ (noted as BKBO) before and after electron beam exposure. Note that after 10 seconds of beam exposure, the diffraction patterns were destroyed. At the same time, BKBO showed hole-shaped microscopic features, implying that the sample became changed in terms of crystal periodicity. As a consequence, the most direct way to investigate a surface termination layer, transmission electron microscope, is unfortunately not applicable to BBO.

In this work, we grew BBO (001) films by pulsed laser deposition (PLD) and adopted *in-situ* ARPES to determine the termination layer and the electronic structures. Observing outgoing photoelectrons with various emission angles, we could obtain the depth profile for spectral-weight ratios of Ba 3*d* to Bi 4*f* core levels. We found that the spectral-weight ratio got smaller when the emission angle became large, which implied that the termination layer was a BiO₂ layer. Thus, we could confirm the termination layer and check whether

our films satisfied the condition for the proposed mechanism by VGL. Using the grown BBO films, we obtained angle-resolved valence band spectra. However, the ARPES spectra did not show any features of metallic states on anywhere in the Brillouin zone (BZ). We found that sophisticated theoretical investigations are needed to study the correct electronic structures of BBO [18].

3.2 Methods

We deposited BBO thin films on doped STO substrates with 1% atomic ratio of Nb, so-called Nb:STO. PLD technique was adopted. We utilized two different PLD-ARPES systems for core-level spectra measurement from various emission angles and angle-resolved valence band spectra. Crystallinity and surface roughness of PLD-grown samples strongly depends on surface quality of substrates, thus we prepared Nb:STO by etching using buffered fluoric acid [19-20]. We used a commercial BBO polycrystalline target (Toshiba Manufacturing Co.) for a target material. The recipe for BBO was adopted from our previous publication [21]. We set the thickness of films as 30 unit cells, thus they were away from the dimensionality crossover [21]. Crystallinity and surface roughness were checked by X-ray diffraction and atomic force microscopy (AFM), respectively. The overall quality of sample characterization was good as our best report [21]. We confirmed that our films had small roughness and step-terrace structures on their surfaces, which supported uniform termination of the grown samples.

We measured core-level spectra using a PHOIBOS-225 electron analyzer (SPECS GmbH)

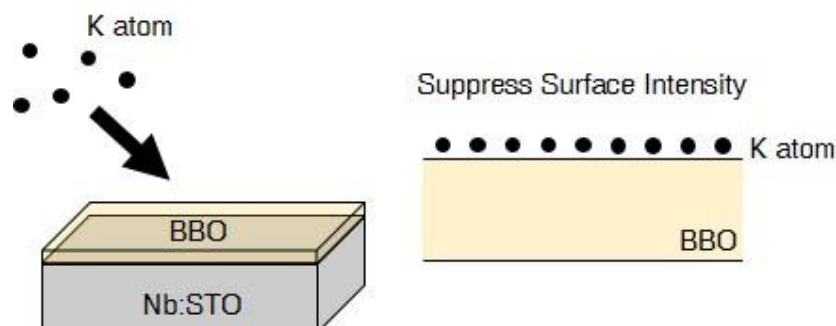


Figure 3.3 *in-situ* K dosing process and mechanism to suppress surface intensity.

with a monochromatic Al $K\alpha$ source ($h\nu = 1486.6$ eV). The grown samples were transferred without exposure to air. Thus, unintended surface contamination by adsorbates was minimized. After the transfer, we set an acceptance angle as 3° along the (001) axis, which is the surface-normal direction, and measured angle-dependent Ba $3d$ and Bi $4f$ core levels. *in-situ* angle-resolved valence band measurements were performed at the Beamline 7.0.2 MAESTRO in the Advanced Light Source. The electron analyzer used for *in-situ* ARPES was a Scienta R4000 electron analyzer at $h\nu = 120$ eV. During all the measurement, vacuum pressure had been kept below 1×10^{-10} Torr for both systems. For successful *in-situ* ARPES measurement, it is important that vacuum status after deposition should be maintained as low as possible. We maintained the vacuum pressure during sample transfer below 1×10^{-9} Torr after we removed samples from the PLD chambers.

We utilized *in-situ* potassium (K) dosing for intentional surface contamination using a commercial alkali metal dispenser (SAES group Co.). The schematic of K dosing was described in Fig. 3.3. It is important to control the K dosing sequence for controlled dosing. Thus, we found control parameters based on the operation manual and empirical results on various samples. When conducting the experiment, the K dispenser was stabilized. After

the stabilization, K atoms were deposited with a constant rate using 5.8 A of current for 35 seconds. We defined this as “one” step. During the K deposition, we had monitored the K $3p$ core level and angle-resolved valence band cut after every single step. The monitoring was for observing any unintended possible contamination and the amount of dosed K atoms. The amount of K dosing was estimated by comparing photoionization cross sections between core levels.

3.3 Result and discussion

3.3.1 Angle-dependent x-ray photoelectron spectroscopy

We described the experimental situations in Fig. 3.4. Deposited BBO (001) films can have two possible terminations as described in the introduction, BiO_2 -layer and BaO -layer. Our purpose is investigating whether a metallic surface state exists as VGL predicted. Hence, we need to confirm the termination layer first. As mentioned in the introduction part, it is not possible to visualize the surface termination layer by electron microscopies [22]. Instead, we adopted *in-situ* core-level x-ray photoelectron spectroscopy (XPS). The key idea was from the finite escape depths of photoelectrons [23]. If a photoelectron with fixed kinetic energy from a specific ion has a constant finite escape depth, the spectral intensity from photoelectron counts will exponentially decreases with the distance that the photoelectron needs to travel to the surface (typically the travel length at widely used

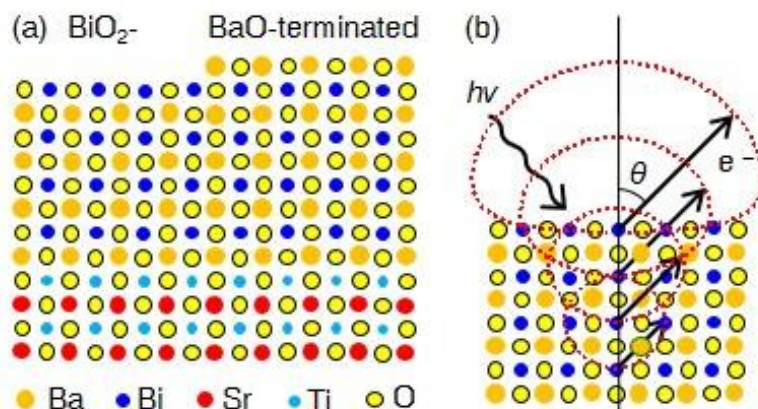


Figure 3.4 An illustration for schematic introduction for our experiments. (a) Two possibilities on the termination layer, BiO₂⁻ and BaO-termination. (b) Photons and photoelectrons from a film. Note that photoelectrons were generated from different depths, which results in reduction in photoelectron intensity. The reason is that generated photoelectrons have finite escape depths. Adopted from [18].

energy range is about a few unit cells). The *effective* travel length has cosine dependence on the emission angle θ (see Fig. 3.4 (b)).

We obtained Ba $3d_{5/2}$ and Bi $4f_{7/2}$ core-level spectra with various emission angles depicted in Fig. 3.4 (b). The spectra were shown in Fig. 3.5. Shirley backgrounds were already removed; thus we could obtain spectral weights from each core level directly.

Note that Bi $4f_{7/2}$ core-level spectra with all emission angles were little asymmetric. There are many reasons which can reproduce the asymmetry; here the reason is the existence of the second component. Basically, the displayed Bi $4f_{7/2}$ spectra showed two components and they are spatially distinguished with each other. That is because the existence of the second component is mainly from spatial separation such as surface/bulk or interface

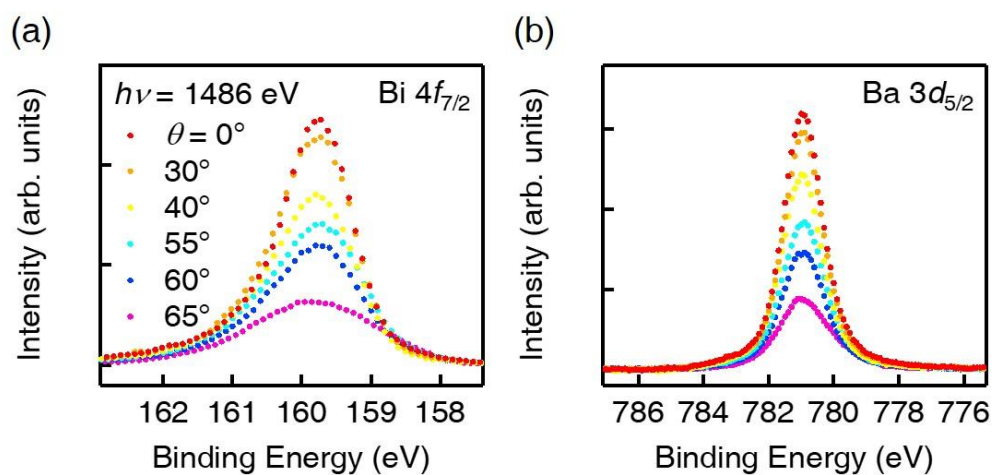


Figure 3.5 (a) Bi $4f_{7/2}$ core levels and (b) Ba $3d_{5/2}$ core levels from different emission angles. Adopted from [18].

geometry. In our case, however, the observed second component was not from the spatial separation because we did not observe angle dependence of spectral-weight ratio between those two components (they may show significant angle dependence if the second component were from the spatial separation). Therefore, we concluded that the two-component structure in the Bi $4f_{7/2}$ spectra were specifically from bulk. Contrary to the Bi $4f_{7/2}$ spectra, Ba $3d_{5/2}$ spectra showed single-component structure. Hence, they were obviously from bulk. This can be additional characterization on the sample quality; the absence of non-uniform signature in both core-level spectra was confirmed.

3.3.2 The experimental and simulated spectral-weight ratios between Bi $4f_{7/2}$ and Ba $3d_{5/2}$

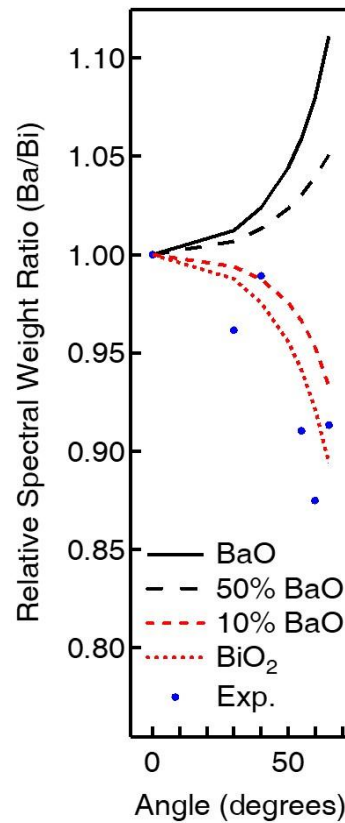


Figure 3.6 Simulated spectral-weight ratios assuming for different situations (black and red solid/dashed lines) and experimental spectral-weight ratio (blue dots). Adopted from [18].

The spectral-weight ratio between Bi $4f_{7/2}$ and Ba $3d_{5/2}$ (S_{Ba}/S_{Bi}) were obtained and described in Fig. 3.6. Qualitatively, the experimental spectral-weight ratio (blue dots in Fig. 3.6) decreased when the emission angle increased. Note that the larger emission angle

brings our measurement to the more surface-sensitive situation. Without quantitative analysis, we could check that the termination layer was governed by a Bi-rich layer. Similar results were reported from thin films grown by molecular beam epitaxy. They were confirmed by time-of-flight scattering and recoil spectroscopy and by mass spectroscopy of recoiled ions [24].

For quantitative analysis, we simulated the spectral-weight ratios with various emission angles. The main assumption for our simulation is that photoelectron intensity (counts) decreases exponentially with a decay constant. The decay constant is derived from the photoelectron mean free path [23]. Let us have A and B layers which alternatively stacked and assume that A is the top-most layer. Then, the spectral weight ratio is given as

$$\frac{S_A}{S_B} = K \frac{\int_0^{\frac{1}{2}} \exp(-\frac{z}{\lambda_A} \cos \theta) dz + \int_1^{\frac{3}{2}} \exp(-\frac{z}{\lambda_A} \cos \theta) dz + \dots}{\int_{\frac{1}{2}}^1 \exp(-\frac{z}{\lambda_B} \cos \theta) dz + \int_{\frac{3}{2}}^2 \exp(-\frac{z}{\lambda_B} \cos \theta) dz + \dots} = K \frac{\lambda_A}{\lambda_B} \frac{1 + \exp(-\frac{1}{2\lambda_B} \cos \theta)}{1 + \exp(\frac{1}{2\lambda_A} \cos \theta)} \quad (3.1)$$

where K is a factor reflecting the concentrations of A and B and their photoionization cross sections. λ_A and λ_B are the mean free paths of the photoelectrons from a particular kinetic energy of photoelectrons. We adopted this spectral-weight simulation to BaO- and BiO₂-terminated BBO. The simulated plots were displayed in Fig. 3.6 as black and red curves. We simulated the ratio with various emission angles to compare with the experimental spectral-weight ratio. λ_A and λ_B were obtained from the NIST Electron Effective-Attenuation Length database and are 22.06 Å and 35.55 Å, respectively. Since the factor K has unknown or hard-to-define parameters, we normalized the simulated and experimental spectral-weight ratio at the normal emission case.

Four different simulation results were depicted in Fig. 3.6. Two realistic probable

termination scenarios (BaO- and BiO₂-terminations) and two imaginary mixed termination scenarios were listed. Overall matching between the experimental and simulated results was the best with the BiO₂-termination case. There were some minor deviations which possibly came from photoelectron diffraction effects [25] or grazing beam incidence. We considered possible inter-contamination between Ba and Bi ions during thin film synthesis. However, the intermixing unlikely happened in our experiments as confirmed by comparison with the imaginary simulations (10% and 50% intermixed BaO). Thus, we confirmed that our films had BiO₂-termination layers.

3.3.3 Constant energy surfaces of BBO

Often spectra from electron spectroscopy has been used for a quality-check (especially

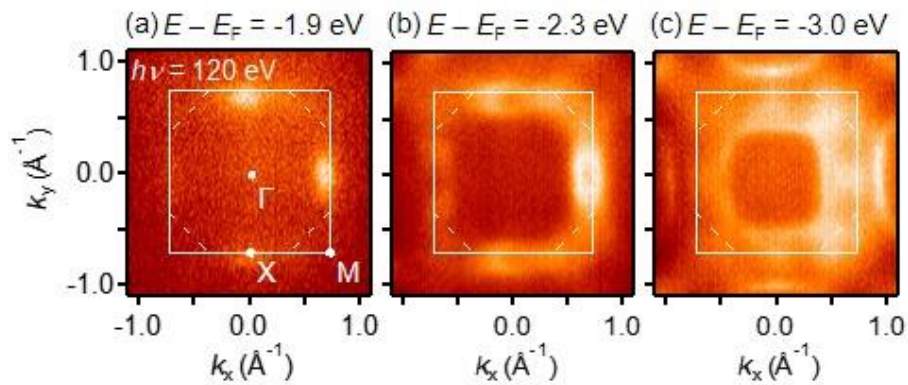


Figure 3.7 Constant energy surfaces below (a) 1.9 eV, (b) 2.3 eV, and (c) 3.0 eV from the Fermi level. Note that the first Brillouin zone (simple cubic zone) and folded zone by crystal structure distortion were indicated as white solid/dashed lines, respectively. Adopted from [18].

surface quality) tool since outgoing electrons will have ill-defined momentum if they undergo inelastic scattering due to surface impurities. In addition, crystallinity of measuring regions can be confirmed. In the sense, we obtained constant energy surfaces (CESs) from BBO. We believed that the feasibility of ARPES experiments provides confirmation on sample quality. Hence, we here compared our CESs and reported ones by Plumb *et al.* [26] to confirm the sample quality and further analysis.

Figures 3.7 (a)–(c) showed the CESs from specific binding energies using $h\nu = 120$ eV. 120 eV of photon energy was used to observe the Γ point. As described in Fig. 3.7, the primitive Brillouin zone (BZ) of BBO is folded from the simple cubic zone. This is due to two different crystal structure distortions; the well-known breathing distortion and rock-salt-type tilting and rotations [27]. In addition, the zone folding is occurring with the CDW modulation with $\mathbf{Q} = (\pi, \pi, \pi)/a$ as demonstrated by Plumb *et al.* We would like to adopt the simple cubic zone notation for convenience hereafter. Note that all CESs demonstrated the correct crystal symmetry including zone-folding. Now, we confirmed that our films had good enough quality for ARPES experiments, and showed the same CESs with the previous report except difference in binding energy nature. The difference will be discussed in detail in the following chapter.

3.3.4 Band dispersions of BBO

In the previous two chapters, we confirmed that our films had BiO_2 -termination layers and were good enough for electron spectroscopy. Therefore, it is ready to investigate the

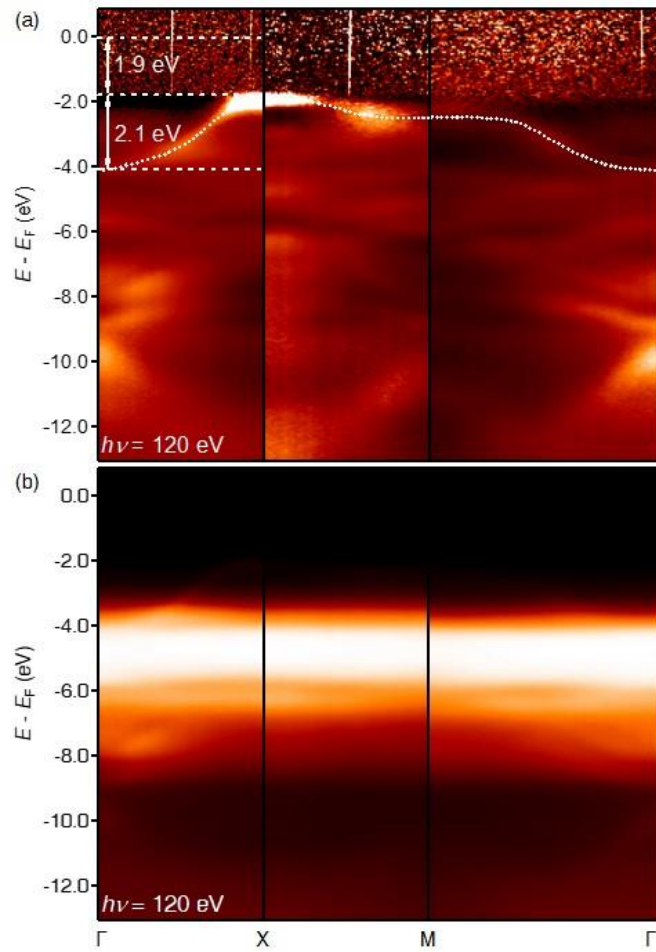


Figure 3.8 ARPES spectra along the $\Gamma X M \Gamma$ line. The high symmetry points were indicated in Fig. 3.7. (a) Normalized spectra by the method describe in the main text. White dashed line is for a guide. The relative energy level and bandwidth of the top-most valence band were also indicated. (b) Raw ARPES spectra. Adopted from [18]. presence of the predicted metallic surface state. We obtained angle-resolved valence band spectra using $h\nu = 120$ eV and displayed on Fig. 3.8. The spectra were taken along the line connecting the high symmetry points indicated in Fig. 3.7 (a). We normalized the spectra

by the maxima and minima of the momentum distribution curves (similar way for the normalization in Ch. 2). The normalization generally clarified band dispersions regardless binding energy compared with the raw spectra. Note that noisy patterns in the normalized spectra (Fig. 3.8 (a)) was due to low spectral intensity in the raw spectra.

We observed the top-most band formed by antibonding between Bi $6s$ -O $2p$ marked as the white dashed line in Fig. 3.8 (a). The maxima and minima of the band was at $E - E_F = -1.9$ eV and -4.0 eV, respectively. Consequently, the bandwidth was 2.1 eV which was 10 % larger than that in a BBO slab calculated by VGL. Since ARPES can observe occupied states, our results explicitly showed that the band gap of BBO should be larger than 1.9 eV. This was consistent with the measured optical gap of 2.0 eV [28-30]. By following the prediction by VGL, there should be a hole pocket at the X point and an electron pocket on the Γ M line as surface states. Our observation from ARPES, however, did not show any hints on both of them near the Fermi level.

As we did for the FS, we also compared our results with the previous report [26]. Overall shape of the dispersions agreed well with each other. Despite the good agreement in the bandwidth, we here note some differences. First, the energy level of the top-most valence band in our ARPES spectra was different from the previously reported spectra. The lowest binding energy at which spectral intensity was observed was 1.9 eV, while Plumb *et al.* observed at the binding energy of 0.3 eV. We traced back the origin of such discrepancy and concluded that different types of pinned impurities could be responsible. The previous work used a SrRuO₃ (SRO) buffer layer to compensate charges in the BBO layer since photoemission measurement needs a charge reservoir (metallic systems do not need a

reservoir, however, BBO is a semiconductor). Thus, their films had BBO/SRO/STO geometry, meanwhile ours had BBO/Nb:STO. It is well-known that SRO films grown by PLD technique often contain Ru vacancies [31] and the vacancies work as charge acceptors. Contrary to Ru vacancies in SRO, metallic Nb:STO is a charge donor due to extra charges from doped Nb. In conclusion, both of them differently work in terms of giving or taking charges from BBO, resulting in different chemical potential pinning. Although the chemical potential location of our result and Plumb et al. showed 1.6 eV difference in energy, the relative position of the top-most band and its bandwidth remained the same. Thus, our result agreed well with the previous report even though the sample geometry was different.

3.3.5 *in-situ* K dosing onto a BBO thin film

Though we confirmed that our results agreed well with the previous report and there was no spectral weight near the Fermi level, it could be not enough to deny the prediction by VGL. This is because a surface state is very fragile to external perturbations such as contamination by adsorbates [32]. To find out the unintended surface contamination effects, we utilized *in-situ* K dosing. As described in the method part, we evaporated K atoms using well-defined sequence. Induced changes by K dosing was observed when K was dosed more than 0.01 monolayer. The observed K-induced change in the band dispersion also indicated that initial surface quality of our films was good since the amount of initially present defects was not enough to induce surface contamination resulting in

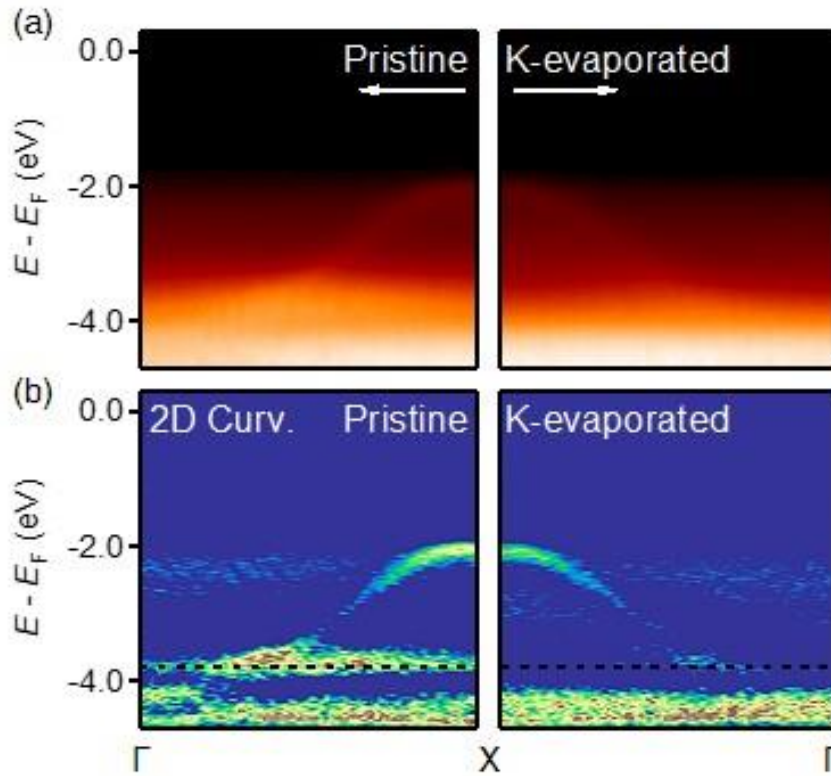


Figure 3.9 (a) Comparison of ARPES between pristine and K doped films (b) the same comparison as we did in (a) by clarifying band dispersions using the two-dimensional curvature method described in the main text. The observed difference is disappearance of a flat band located at -3.8 eV marked by a black dashed line. Adopted from [18].

band structure changes. The final deposited amount of K was about 0.1 monolayer as confirmed by a comparison of spectra weight between K $3p$ and Ba $5p$ core levels considering photoionization cross sections of both core levels [33].

We displayed the ARPES spectra from the pristine and K-evaporated BBO films in Fig. 3.9. Figure 3.9 (a) showed raw ARPES spectra of pristine and K-evaporated films. Since

the change before/after K dosing was hard to recognize by eyes, we applied the two-dimensional curvature method to clarify dispersions [34]. There is a flat band located at -3.8 eV in the pristine film as marked by a black dashed line in the right panel of Fig. 3.9(b). Contrary to the pristine film case, the K-evaporated film did not show the flat band. Note that except the flat band, the dispersive top-most valence band still exist in both pristine and K-evaporated films. In addition, we did not observe any rigid band shift or formation of any electron/hole bands indicating there was negligible effect in charge transfer from dosed K.

The flat band disappeared without any shift in energy when we increased the amount of

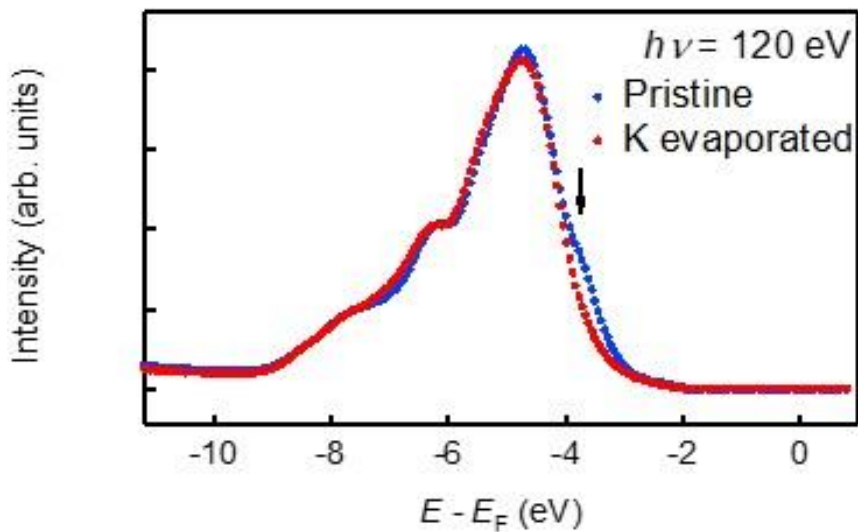


Figure 3.10 Angle-integrated spectra from pristine and K evaporated films. Spectral intensity -3.8 eV is suppressed, which was consistent with the disappearance of the flat band observed in Fig. 3.9. There was no change near the in-gap region even we magnified the spectra 100 times. Adopted from [18].

dosed K. It just got faint and did not show any shift in energy or momentum axis. In an angle-integrated spectrum in Fig. 3.10, we could confirm that spectral intensity at -3.8 eV suppressed after K dosing. Such disappearance of a band is related with presence of a surface band. The flat bands were also observed by the study of VGL near the bottom of the topmost valence band. We also cross-checked that there was no metallic state by analyzing an angle-integrated spectrum shown in Fig. 3.10. There was no spectral intensity near the Fermi level in both pristine and K-evaporated films.

3.3.6 Absence of a metallic surface state: oversimplified band calculations

The important issue here is understanding the absence of a metallic surface state. We attributed the absence of a metallic surface state to the oversimplified band calculations. Franchini *et al* demonstrated that calculation results for electronic structures depend on choices of exchange correlation functionals or calculation methods [35]. Local density approximation or generalized gradient approximation predicted semimetallic ground states [36]. The main idea was that various calculated band-gap values predicted by such functionals, which clearly contradicts with experimental observations, were due to self-interaction correction for Bi 6s electrons. Bi 6s orbitals are spatially larger than other valence band orbitals, thus with conventional exchange-correlation functionals screening by such large orbitals may be overestimated [37]. The estimation for band-gap values from calculations can be improved by adopting hybrid functionals [38]. Even though hybrid

functionals gave finite band gaps, the size of the gaps were still smaller than the lower bound of 1.9 eV that we observed from ARPES spectra. The underestimated band-gap values from calculations directly show some limitations. In addition, we should take possibility of surface octahera distortion into account. This reconstruction often happens for releasing energy gains from surface discontinuity. For BBO, such possibility for surface reconstruction was not considered; it needs to be investigated further to study surface electronic/crystal structures of BBO in detail.

We would like to end this chapter with some notes for deviations. First, we observed it in the study of VGL that the electron and hole pockets formed by surface bands located 0.4 eV below the bulk conduction band and 0.3 eV above the bulk valence band. This naturally show that the predicted surface bands cannot reach Fermi level to form 2DEGs because the observed band gap should be larger than 1.9 eV. Second, we did not observe the surface band from Bi^{3+} which should occupy the top of the surface valence band. The absence of the surface band from Bi^{5+} could be possibly located well above the Fermi level thus we could not observe it. This is, however, not the case of the surface band from Bi^{3+} . Third, one may argue that there could be the matrix-element effects in our ARPES spectra, thus the predicted surface bands were not observable. However, the predicted surface bands had the same symmetry, and there was no noticeable change from either horizontal or vertical polarization (not illustrated). Finally, we would like to mention the finite-size effect of the calculations. For the electronic structure calculation for a 9-layer slab by VGL, the Bi^{3+} surface band was not clearly separated from the bulk band. This may be responsible for the absence of the surface band. Contrary to this case, in 13-layer

slab calculation, the surface band became separated from the bulk valence band and it originated from the second BiO₂ layer. Therefore, we can conclude that the finite-size effects would be strong in the 9-layer slab calculation. All the notes suggest that more sophisticated approaches are needed to resolve such issues.

3.4 Conclusion

Using *in-situ* photoemission spectroscopy, we investigated the possibility of metallic surface states in BiO₂-terminated BBO films. We determined termination layers of our BBO films from the comparison between Ba 3*d* and Bi 4*f* core-level spectra. We found that our BBO films had BiO₂ termination layers as the condition suggested by the theoretical prediction. Metallic surface states, however, were not observed. Contrary to the expectation, surface states were observed −3.8 eV below the Fermi level, which was also predicted by VGL. The states at −3.8 eV was the lowest energy state among the observed surface states, and we checked it with *in-situ* K deposition. We suggested that more accurate theoretical approaches are needed to study the electronic structures of BBO.

References

- [1] E. Abrahams, S. V. Kravchenko, M.P. Sarachik, *Rev. Mod. Phys.* **73**, 251 (2001)
- [2] A. Ohtomo, H.Y. Hwang, *Nature* **427**, 423 (2004).
- [3] Y.J. Chang, L. Moreschini, A. Bostwick, G.A. Gaines, Y.S. Kim, A.L. Walter, B. Freelon, A. Tebano, K. Horn, E. Rotenberg, *Phys. Rev. Lett.* **111**, 126401 (2013).
- [4] S. Stemmer, S. James Allen, *Annu. Rev. Mater. Res.* **44**, 151 (2014).
- [5] N. Reyren, S. Thiel, A.D. Caviglia, L. Fitting Kourkoutis, G. Hammerl, C. Richter, C.W. Schneider, T. Kopp, A.S. Rüetschi, D. Jaccard, M. Gabay, D.A. Muller, J.M. Triscone, J. Mannhart, *Science* **317**, 1196 (2007).
- [6] A. Brinkman, M. Huijben, M. Van Zalk, J. Huijben, U. Zeitler, J.C. Maan, W.G. Van Der Wiel, G. Rijnders, D.H.A. Blank, H. Hilgenkamp, *Nat. Mater.* **6**, 493 (2007).
- [7] A. Tebano, E. Fabbri, D. Pergolesi, G. Balestrino, E. Traversa, *ACS Nano*. **6**, 1278 (2012).
- [8] E. Assmann, P. Blaha, R. Laskowski, K. Held, S. Okamoto, G. Sangiovanni, *Phys. Rev. Lett.* **110**, 078701 (2013).
- [9] S. Uchida, K. Kitazawa, S. Tanaka, *Phase Transit.* **8**, 95 (1987).
- [10] B.A. Baumert, *J. Supercond.* **8**, 175 (1995).
- [11] A. W. Sleight, *Phys. C* **514**, 152 (2015).
- [12] G. U. Kulkarni, V. Vijaykrishnan, G. R. Rao, R. Seshadri, C. N. R. Rao, *Appl. Phys. Lett.* **57**, 1823 (1990).
- [13] V. Vildosola, F. Güller, A.M. Llois, *Phys. Rev. Lett.* **110**, 206805 (2013).

- [14] Z. Zhang, J. T. Yates, Chem. Rev. **112**, 5520 (2012).
- [15] A. Kalabukhov, R. Gunnarsson, J. Börjesson, E. Olsson, T. Claeson, D. Winkler, Phys. Rev. B **75**, 121404(R) (2007).
- [16] V. E. Alexandrov E. A. Kotomin, J. Maier, R. A. Evarestov, J. Chem. Phys **129**, 214704 (2008).
- [17] I. I. Mazin, d. I. Khomskii, R. Lengsdorf, J. A. Alonso, W. G. Marshall, R. M. Ibberson, A. Podlesnyak, M. J. Martínez-Lope, M. M. Abd-Elmeguid, Phys. Rev. Lett. **98**, 176406 (2007).
- [18] J. S. Oh, M. Kim, G. Kim, H. G. Lee, H. K. Yoo, S. Sinn, Y. J. Chang, M. Han, C. Jozwiak, A. Bostwick, E. Rotenberg, H.-D. Kim, T. W. Noh, Curr. Appl. Phys. **18**, 658 (2018).
- [19] M. Kawasaki, K. Takahashi, T. Maeda, R. Tsuchiya, M. Shinohara, O. Ishiyama, T. Yonezawa, M. Yoshimoto, H. Koinuma, Science **266**, 1540 (1994).
- [20] M. Lippmaa, K. Takahashi, A. Ohtomo, S. Ohashi, T. Ohnishi, N. Nakagawa, T. Sato, M. Iwatsuki, H. Koinuma, M. Kawasaki, Mater. Sci. Eng. **56**, 111 (1998).
- [21] G. Kim, M. Neumann, M. Kim, M.D. Le, T.D. Kang, T.W. Noh, Phys. Rev. Lett. **115**, 226402 (2015).
- [22] P. Patnaik, *Handbook of Inorganic Chemical Compounds* (McGraw-Hill, New York, 2003).
- [23] D. Briggs, M. Seah, *Practical Surface Analysis by Auger and X-Ray Photoelectron Spectroscopy* (John Wiley and Sons Ltd., Chicester, 1983).
- [24] A. Gozar, G. Logvenov, V.Y. Butko, I. Bozovic, Phys. Rev. B **75**, 201402(R) (2007)

- [25] C. Fadley, *Phys. Scr.* **T17**, 39 (1987).
- [26] N.C. Plumb, D.J. Gawryluk, Y. Wang, Z. Ristić, J. Park, B.Q. Lv, Z. Wang, C.E. Matt, N. Xu, T. Shang, K. Conder, J. Mesot, S. Johnston, M. Shi, M. Radović, *Phys. Rev. Lett.* **117**, 037002 (2003).
- [27] D.E. Cox, A.W. Sleight, *Solid State Commun.* **19**, 969 (1976).
- [28] H. Sato, S. Tajima, H. Takagi, S. Uchida, *Nature* **338**, 241 (1989).
- [29] R. Lobo, F. Gervais, *Phys. Rev. B.* **52**, 294 (1995).
- [30] T. Nishio, J. Ahmad, H. Uwe, *Phys. Rev. Lett.* **95**, 176403 (2005).
- [31] W. Siemons, G. Koster, A. Vailionis, H. Yamamoto, D. Blank, M. Beasley, *Phys. Rev. B.* **76**, 075126 (2007).
- [32] K. Park, J.J. Heremans, V.W. Scarola, D. Minic, *Phys. Rev. Lett.* **105**, 186801 (2010).
- [33] J.J. Yeh, I. Lindau, *At. Data Nucl. Data Tables* **32**, 1 (1985).
- [34] P. Zhang, P. Richard, T. Qian, Y.M. Xu, X. Dai, H. Ding, *Rev. Sci. Instrum.* **82**, 043712 (2011).
- [35] C. Franchini, A. Sanna, M. Marsman, G. Kresse, *Phys. Rev. B.* **81**, 085213 (2010).
- [36] T. Thonhauser, K.M. Rabe, *Phys. Rev. B* **73**, 212106 (2006).
- [37] Z. P. Yin, A. Kutepov, G. Kotliar, *Phys. Rev. X* **3**, 021011 (2013).
- [38] J. Paier, R. Hirschl, M. Marsman, G. Kresse, *J. Chem. Phys.* **122**, 234102 (2005).

Chapter 4

Spectroscopic Investigation on Itinerant/Local Magnetism in SrRuO₃

4.1 Introduction

Magnetism is one of the most fundamental and important topics among condensed matter physics, especially its relationship with electronic correlation. The question is how the electronic correlation induces magnetic moments and orders. Considering electrical properties, magnetism in metallic systems has attracted much attentions [1-3]. The most well-known driving mechanism for metallic magnetism is Stoner magnetism pointed out by Stoner [4]. In the Stoner picture, the repulsive Coulomb interaction between itinerant electrons leads to spontaneous spin-splitting. Thus, the key parameters of the Stoner model are the strength of repulsive interaction, of course, and density of states (DOS) at the Fermi level, $D(E_F)$. The Stoner model is successful for describing the basic features of the electronic structures of elemental metallic ferromagnets such as Fe, Co Ni [2]. More importantly, their magnetic environments are not explained well by the famous local model for magnetism, Heisenberg-type spin-spin interaction [2].

SrRuO₃ (SRO) is one of the most attractive perovskite oxides. Its ground state at the

lowest temperature is ferromagnetic and metallic and the Curie temperature (T_C) is 150–160 K (depending on sample quality) [5]. Due to the unique ferromagnetism with metallicity, SRO has drawn notable theoretical and experimental attention [6-10]. One of the questions is whether itinerant ferromagnetism can emerge even though the distance between transition metal ions is about twice compared to that of well-known itinerant ferromagnets (Fig. 4.1). Adopting those physical properties as a component for device applications has been also widely considered and utilized [11-15]. The verification on the origin of metallic ferromagnetism in SRO, however, has not been finished at this moment despite considerable efforts. Various approaches to understand the metallic ferromagnetism have been made through density functional theory (DFT) [6], optical investigations

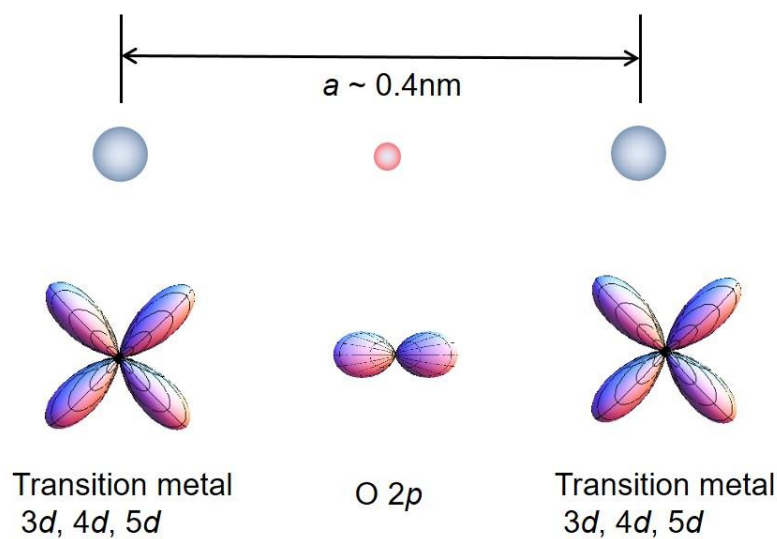


Figure 4.1 A schematic illustration of the distance between transition metal ions in perovskite oxides. Note that in a well-known ferromagnet BCC Fe the distance between the nearest neighbor is about 0.287 nm.

including magneto-optical Kerr effect [7-8], and angle-resolved photoemission spectroscopy (ARPES) [9]. Although some of the previous reports contributed to understand the basic description on the electronic structure of SRO, clear evidence or theory for a unified picture has not been found.

Lack of experimental description for the momentum-resolved electronic structure of SRO has been obscuring our understanding. The early DFT reported that the DOS of SRO at the Fermi level was large enough to satisfy the condition for Stoner magnetism [6]. Even though the structure distortion was considered, ferromagnetic ground state was reproduced. However, the magneto-optical Kerr effect measurement observed that there was no significant energy change across the ferromagnetic-to-paramagnetic transition, thus local spin-spin interaction should be responsible [7]. After those early works, some advanced studies were made after 2013. Temperature evolution of optical spectrum of SRO thin films was reported and it supported that Stoner-like temperature dependence was dominant below T_C [8]. Surprisingly, there was still additional evolution above T_C , which might be from local fluctuation of local moments. Therefore, the temperature-dependent optical spectra suggested possibility of coexistence of local and itinerant magnetism in SRO.

Let us explain in detail on the first momentum-resolved electronic structure report on the SRO, one of the most recent studies, by Shai *et al* [9]. Their key finding was displayed in Fig. 4.2. Additional to their first report on Fermi surface (FSs) and band dispersions of SRO, they obtained temperature-dependent band dispersions. A kink structure was found at the binding energy of 65 meV, but they focused on the peak found at the binding energy of 200 meV. Maxima in momentum distribution curves (MDCs) were pointed out in Fig. 4.2 (c),

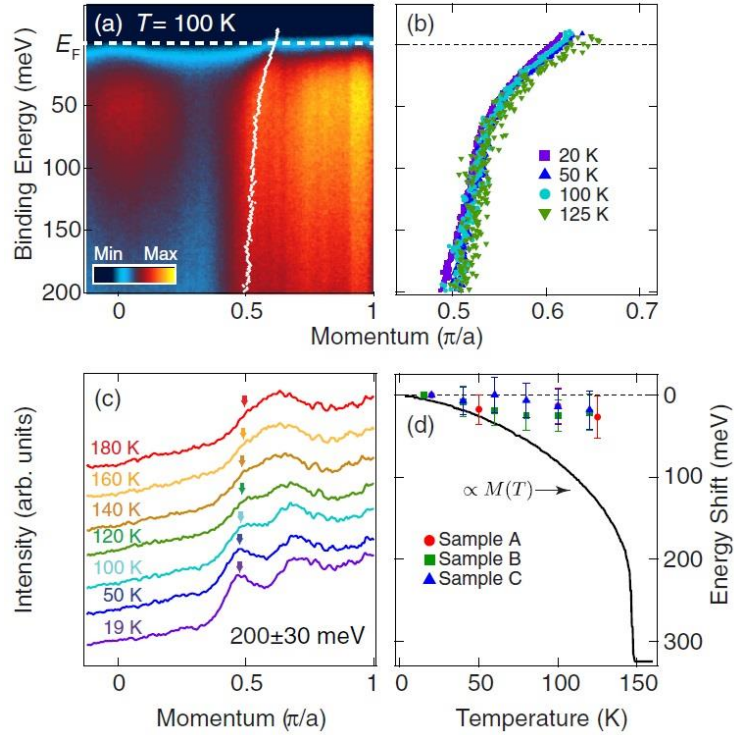


Figure 4.2 (a) Momentum-resolved band structure of SRO at 100 K. (b) Intensity maxima plots in momentum distribution curves. (c) Temperature-dependent peak positions in momentum distribution curves at $E - E_F = 200$ meV. (d) Energy shift of the annotated peak in (c) Temperature-dependent magnetization curve shape was also displayed for comparison. Adopted from [9].

and the relative energy shifts were calculated by multiplying slopes of the band dispersion ($\partial E/\partial k$). Comparing with temperature-dependent magnetization, the energy shift was negligible, which contradicted the Stoner picture. Thus, they supported that a role of local magnetic moments was important. Their work is the first report on ARPES spectra on SRO, thus it provided useful information and electronic structure description. However, since

they adopted a He I source, they cannot verify the exact k_z where they observed. In addition, the reason why they choose the binding energy of 200 meV as exchange splitting was not justified. Overall, though their pioneering work reported a useful description, detailed understanding for the electronic structure and the metallic magnetism of SRO still needed improvement.

Here, we experimentally provided the three-dimensional (3D) momentum-resolved electronic structure by ARPES for the first time. We successfully located high symmetric planes in the Brillouin zone (BZ), mapped FSs, and obtained band dispersions. Our finding opened a way for verifying theoretical arguments that have been made over 20 years so far. By comparing our results with calculations, we showed that the exchange splitting from ferromagnetism did not completely become zero even above the T_C . This is critical experimental evidence for the dual origin in ferromagnetism of SRO. The duality can be a consequence of local correlation as well as dynamic screening in $4d$ transition metal oxides.

4.2 Methods

Single-crystalline SRO samples were synthesized by the reported recipe [5]. The perovskite crystal structure has no preference on a cleavage plane, thus conventional *in-situ* cleaving for SRO results in a micron-scale rough surface. Thus, if the beam is not small enough, ARPES measurement is not probable due to surface roughness. SRO samples were attached to flat copper pucks for ARPES measurements. A microscope image of attached samples was shown in Fig. 4.3. To enlarge the cleaved surface, we scratched sides of SRO

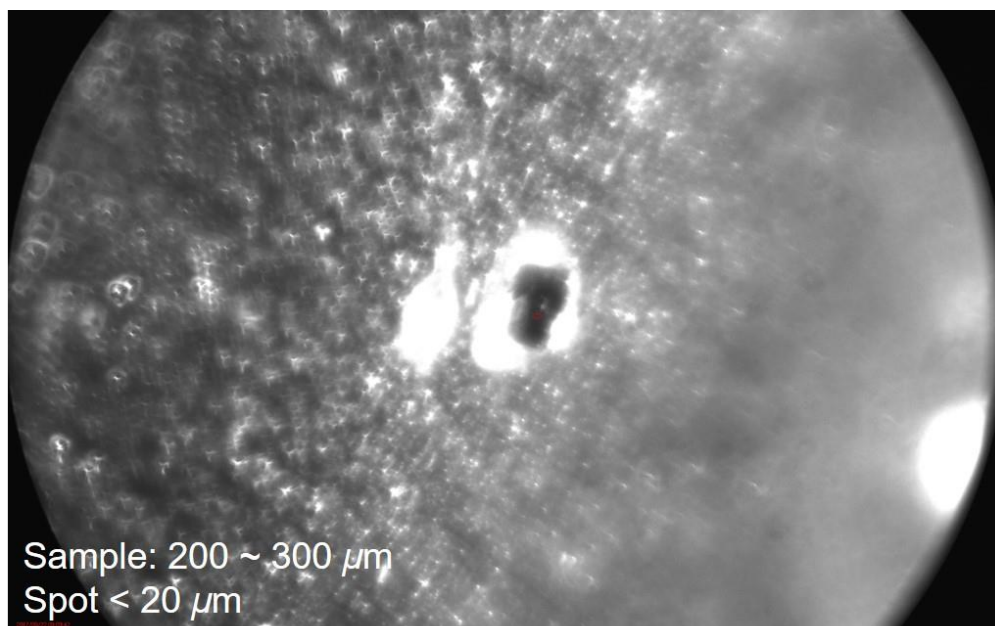


Figure 4.3 A microscope image of a SRO single crystal on a copper puck for ARPES measurement.

crystal flakes. A typical length of one side of a resulting cleaved surface was 10–200 μm .

We conducted photoemission measurement using the endstation installed at the Beamline 7.0.2 MAESTRO in the Advanced Light Source. We can directly observe the sample via a microscope during all measurement, therefore it provided a particular advantage for our experimental procedure. In addition, a home-built 6-axis manipulator provided accurate sample motion for alignment. The beam size could be focused down to $10 \times 12 \mu\text{m}^2$, which was also essential for the measurement. We used a Scienta R4000 electron analyzer at various photon energies for specific purpose. Vacuum during the measurement had been kept below 3×10^{-11} Torr to prevent unintended surface contamination. In all photoemission measurement, sample temperature was kept at 35 K if there is no specific

indication. For temperature-dependent measurement, we cross-checked temperatures by fitting angle-integrated spectra using the Fermi-Dirac distribution function. An ellipsoidal undulator (EPU) was used to control the polarization of synchrotron radiation. We utilized two different polarizations, linear horizontal (LH) and linear vertical (LV).

We utilized *in-situ* potassium (K) dosing for intentional surface contamination using a commercial alkali metal dispenser (SAES group Co.). After the K deposition, we had monitored the K $3p$ core level and angle-resolved valence band cut. The monitoring was for observing any unintended possible contamination and the amount of dosed K atoms. The amount of K dosing was estimated by comparing photoionization cross sections between core levels.

4.3 Result and discussion

4.3.1 k_z dispersion of the electronic structure of SRO

One of our experimental advantages was from a degree of freedom to pick up a desired photon energy. By mapping FSs with various photon energy, we could determine an inner potential and locate high symmetry planes in the BZ. To determine the inner potential, we first obtained Fermi surfaces over a period in the BZ. Note that we adopted conventional simple cubic zone scheme though the crystal structure of SRO is orthorhombic due to tilting and rotation of RuO_6 octahedra [5]. If we have c-axis lattice parameter, then a half of BZ periodicity is obtained (denote it as π/a). Now, the inner potential V_0 can be determined by

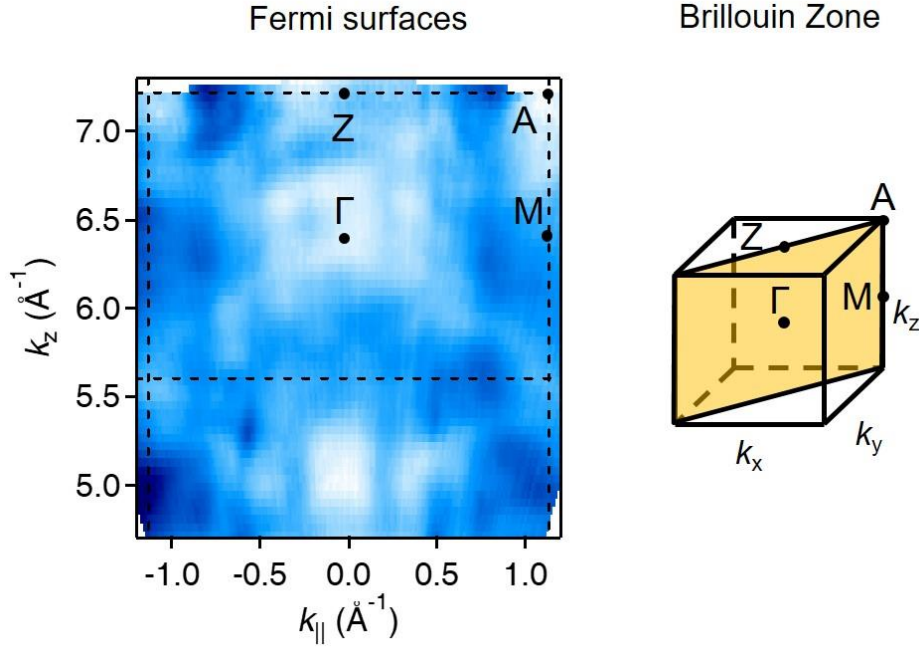


Figure 4.4 A Fermi surface map obtained with various photon energies. We used an energy step of 2 eV. The probing plane in reciprocal space is marked in the right panel. The solid black boundary indicated the simple cubic BZ boundary.

numerically solving an equation below from two kinetic energies which observe Γ (BZ center) and Z (BZ boundary).

$$\frac{\pi}{a} = \sqrt{\frac{2m}{\hbar^2}} (\sqrt{E_{kin,Z} + V_0} - \sqrt{E_{kin,\Gamma} + V_0}) \quad (4.1)$$

where $E_{kin,Z}$ and $E_{kin,\Gamma}$ are measured kinetic energies of photoelectrons which observe Z and Γ points, respectively (Note that they does not have to be exact Z and Γ points. They only need to observe paths spacing a half of reciprocal lattice).

Figure 4.3 showed a photon energy scanning map. The sample was azimuthally rotated

by 45 degrees. The probing plane in reciprocal space is marked in the right panel. Although the map was blur to notify detailed features, we could determine a period in the BZ. By determining a period (or a half), now we could numerically solve the equation 4.1 for the inner potential V_0 . The determine V_0 was about 14 eV. The horizontal and vertical axes in Figure 4.3 were already converted into a unit reciprocal space by the determine inner potential. Finally, we could determine planes where high symmetric points lie on. $h\nu = 147$ eV can observe the BZ center (Γ XM plane) and $h\nu = 113$ eV can determine the BZ boundary (ZRA plane).

After converting the photon energy scan map into the k_{\parallel} - k_z map, 3D dispersive electronic structures were revealed. Along the $k_{\parallel} = 0$ line, spectral intensity almost disappeared at the center of the BZ and appeared again near the zone boundary. Along the $k_{\parallel} = 1.13 \text{ \AA}^{-1}$ (zone boundary) line, spectral intensity behaves in the opposite way. However, there are also some two-dimensional (2D) line shape dispersions parallel to the k_z axis. This quasi-2D dispersions would be consistent with the band dispersions observed in Sr_2RuO_4 [16]. To investigate the origin of quasi-2D and 3D bands, we need to analysis orbital characters.

4.3.2 Fermi surfaces of SRO

Since we determined V_0 and photon energies that enabled us to measure FSs on the high symmetry planes (zone center and boundary), we obtained FSs on the Γ XM plane and ZRA plane, which has remained unexplored so far. Figure 4.5 showed the obtained FSs. Figure 4.5 (a) showed FSs on the Γ XM plane. Overall Fermiology seems very similar

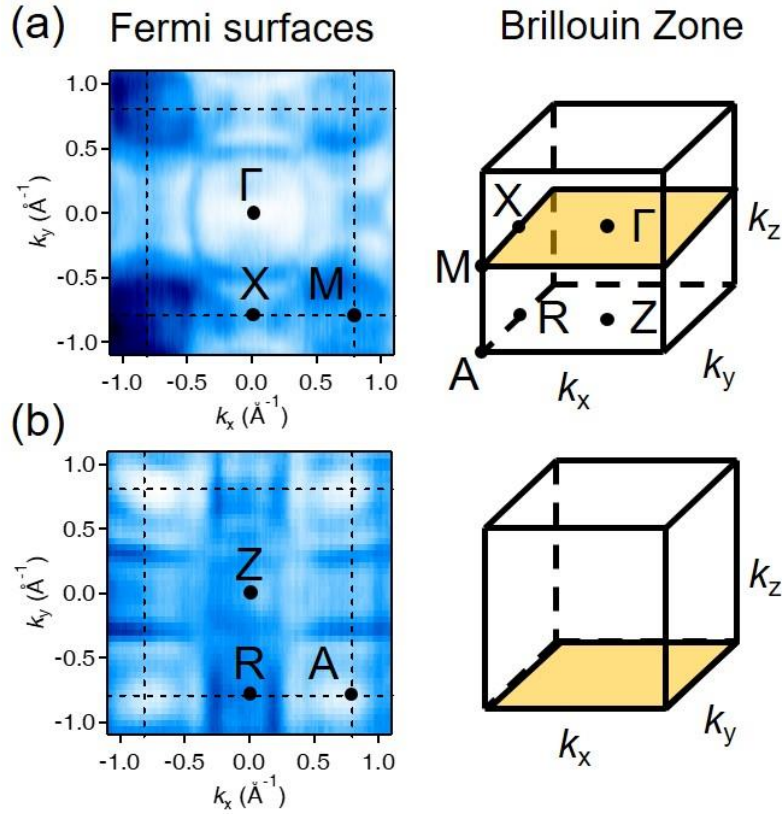


Figure 4.5 Measured FSs on (a) the Γ XM plane and (b) ZRA plane. The BZ boundaries on each map were indicated as black dashed lines. They showed significant difference indicating 3D dispersive nature in the electronic structure of SRO. The measuring regions in the first BZ were shown in the right panels.

with that of Sr_2RuO_4 [17]. Four small hole pockets located at each corner of the simple cubic BZ. The hole pockets have analogy with the α band in Sr_2RuO_4 . Near the hole pockets, faint lobe-shaped spectral intensity was observed. From a different point of view, the lobe might be considered as a big electron pocket centered at the Γ point. This has consequence of the γ band in Sr_2RuO_4 . Last spectral feature in Fig. 4.5 (a) was a rounded

square centered at the Γ point. The band might be formed similarly as the β band in Sr_2RuO_4 did.

The Fermiology on the ZRA plane was notably different from that on the ΓXM plane. Main spectral features on the ZRA plane were lines and four small hole pockets were formed at each corner. The hole pockets were quasi-2D since they were also observed on the ΓXM plane. This observation was consistent with the k_{\parallel} - k_z map (Fig. 4.4) obtained in the previous chapter. We will analyze the line-shaped features parallel to the k_x (or k_y) axis in detail later.

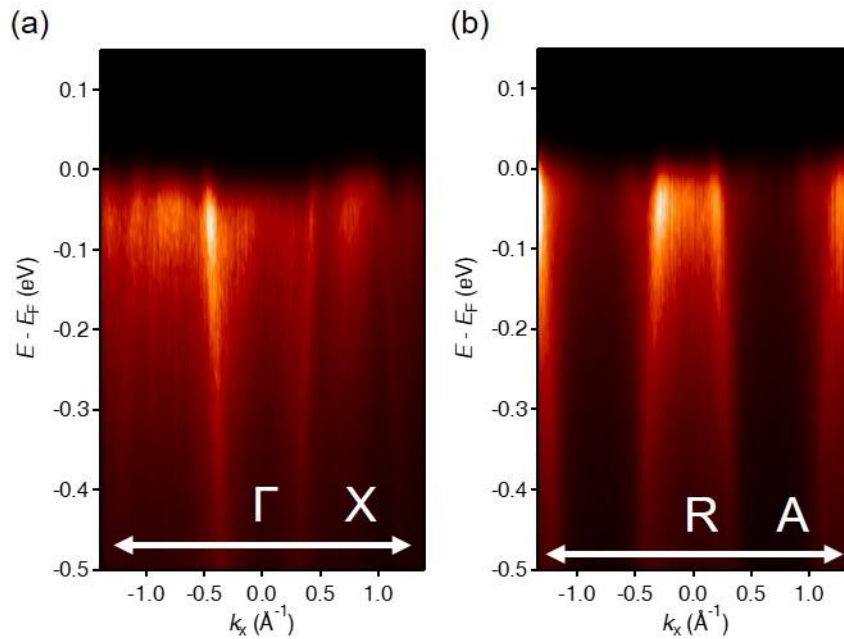


Figure 4.6 (a) Band dispersions obtained along the ΓX line and (b) RA line. Notation and specific location of high symmetric points were marked in Fig. 4.5.

4.3.3 Band dispersions of SRO

We measured band dispersions of SRO along the high symmetric points. Figure 4.6 showed some of the dispersions. Though we did not list all the high symmetry lines in the BZ, two dispersions showed main aspects that we need to focus on. Figure 4.6 (a) showed the band dispersions along the ΓX line, Thus the sharp band was from the β band and faint band approximately centered at X point was from the γ band. The β band showed a kink at around 60 meV, which was reported by the previous work [9]. Additional to the β and γ band, there was also faint spectral feature near the Γ point. In the FS map, the feature near the Γ point was negligible in intensity. By those observation, we concluded that this can be a remnant of folded bands by crystal structure distortion. Thus, considering the folding patterns in orthorhombic structure compared to simple cubic structure, the folded band should be from the γ band.

On the RA cut, there was a hole band centered at the R point. By comparison with the FS map illustrated in Fig. 4.5 (b), the bright hole band had almost straight shape parallel to the k_x (k_y) axis. It meant that that band was almost dispersionless along the k_x (k_y) axis. Contrary to the FS map in Fig. 4.5 (b), the bright band showed dispersive characteristic in Fig 4.4. Note that the α and β bands in the ΓXM plane were resulted from hybridization between two straight bands and each of them was parallel to the k_x and k_y . Thus, the initial (before hybridization) bands were straight as observed in the ZRA plane. In conclusion, the straight spectral features observed in Fig. 4.5 (b) was dispersionless along the k_x or k_y axis, thus they were quasi-2D though they were dispersive along the k_z axis.

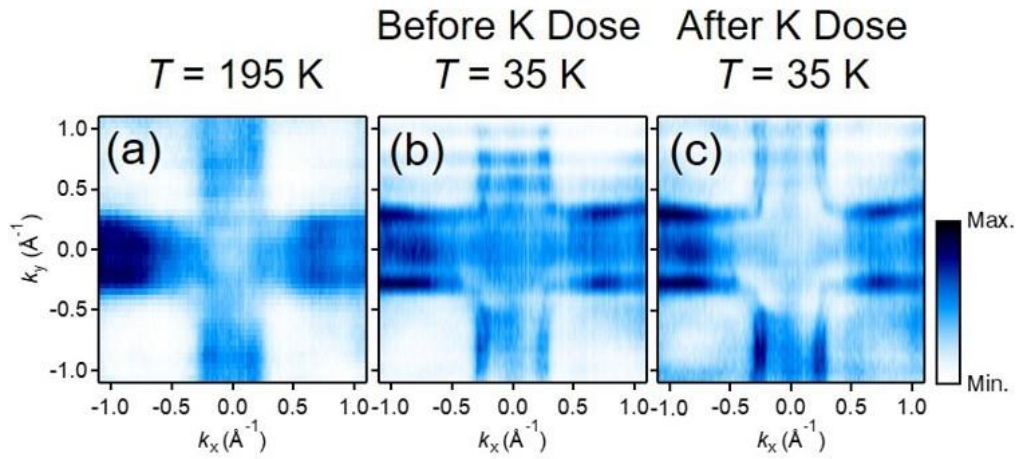


Figure 4.7 (a) A FS map on the ZRA plane at $T = 195$ K. **(b)** Another FS map on the same reciprocal space region at $T = 35$ K. Note that the straight spectral feature now became split into two lines. **(c)** the same FS map with **(b)** obtained after *in-situ* K dosing.

We would like to note some details. First of all, there were weak bands at the midpoint between R and A points in Fig. 4.6 (b). They were easier to observe in the FS map in Fig. 4.5 (b). The zone folding formed spectral intensity near the Z point by folding these weak bands. The folded band was observable as a faint small feature near the Z point in Fig 4.5 (b). Secondly, there was also notable spectral intensity at the R point. This was not from the zone folding as the band at the Z point did. This is because the R point still stays in the first BZ even the zone folding was considered. We investigated how this faint band formed and it was related with other bands in the following chapter.

4.3.4 Temperature and polarization dependence of Fermi surfaces of SRO

Since SRO has ferromagnetic transition at 160 K, we studied temperature evolution, we first studied the temperature evolution of the electronic structures of SRO across T_C increasing both energy and momentum resolutions compared to the FS map obtained in Fig. 4.6. By the enhancement, temperature dependence of FSs on the ZRA plane was revealed. Figure 4.7 (a) showed a FS map on the ZRA plane at $T = 195$ K. Overall Fermiology was similar with the shown FS in Fig. 4.6 (b). The broad FSs might be from thermal broadening effect. When we decrease the temperature below T_C , the FSs showed a notable change. As shown in Fig. 4.7 (b), the straight FS now became split into two parallel straight lines. This has never been observed so far from ARPES [9] and quantum oscillation measurements [18-19]. Additional to the small splitting, separation between broad FS almost exactly at

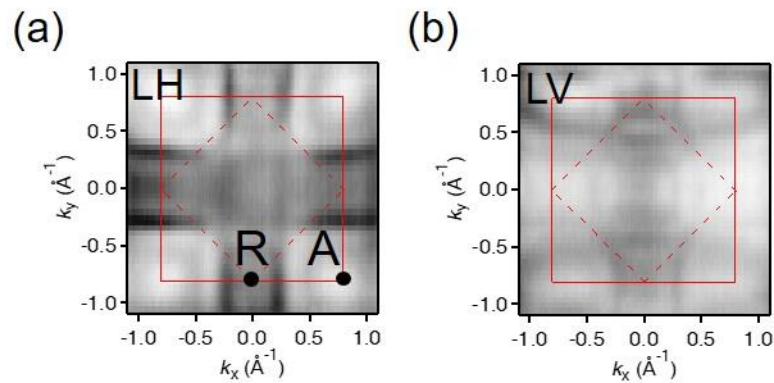


Figure 4.8 (a) A FS map on the ZRA plane with LH-polarized radiation and (b) LV-polarized radiation.

the R point and the shape split band became significant in the low temperature.

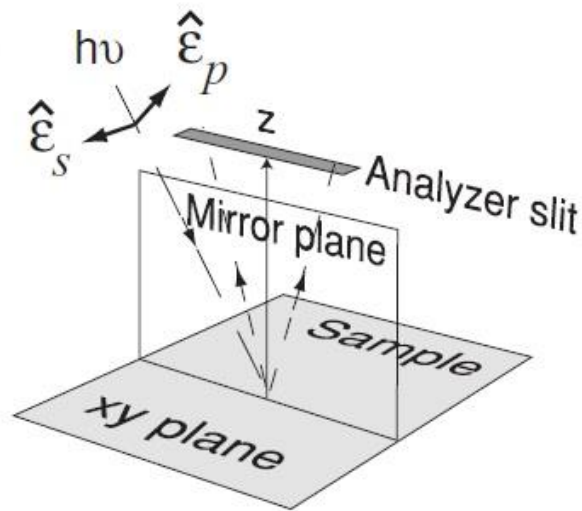


Figure 4.9 Experimental geometry of polarization dependent ARPES measurement. Adopted from [20].

ARPES has been adopted as one of the most important experimental techniques for detecting surface states. Such a small splitting as we observed in Fig. 4.7 (b) is often assigned as a small shift with respect to a bulk state. For Sr_2RuO_4 , in an up-to-date high resolution FS map we could observe surface-originated splitting, which also suggest possibility of coexistence of surface/bulk states on an experimentally obtained FS map. To exclude this scenario, we performed *in-situ* K dosing to suppress possible surface states. A FS map obtained after the K dosing was shown in Fig. 4.7 (c). Note that there was no notable charge transfer from *in-situ* K dosing since the overall shape of the FS remained almost the same. Focusing on the small splitting, we did not observe suppression on one of the split bands or merging. This indicated that both split bands were from bulk states.

To obtain information of orbital characters of topmost valence bands which determine the FS, we obtained FS maps on the ZRA plane using LH and LV polarizations. Figure 4.8 showed FS maps obtained using LH and LV polarizations. Overall spectral intensity from the FSs was stronger in the map from LH polarization. The map from LV polarization showed some features, however, all the FSs signatures were weak. The straight shaped spectral features were significant under LH polarization.

Determining orbital characters from polarization dependence measurement needs a careful examination on the experimental geometry. Since the ARPES intensity depends on the so-called matrix element effect, polarization vector and orbital characters that we are observing affect the matrix term. The matrix element $M_{f,i}^{\vec{k}}$ has relation as

$$M_{f,i}^{\vec{k}} \propto \left| \left\langle \phi_f^{\vec{k}} \left| \hat{\epsilon} \cdot \vec{r} \right| \phi_i^{\vec{k}} \right\rangle \right|^2 \quad (4.2)$$

where $\hat{\epsilon}$ is an unit vector of the electric field of radiation (thus, the direction of polarization). $\phi_i^{\vec{k}}$ and $\phi_f^{\vec{k}}$ are the initial and final states, respectively. The final-state wavefunction can be approximated as a plane-wave for sufficient high photoelectron kinetic energy. Thus, it always remained parity-even until the assumption is valid. $M_{f,i}^{\vec{k}}$ is now dependent on the parities of the polarization and the initial-state. Both of them should have the same parity (all-even or all-odd) to produce non-zero $M_{f,i}^{\vec{k}}$.

In SRO, three d orbitals build the top-most valence band. By crystal field splitting in RuO_6 octahedron environment, five d orbital levels become split into 3 t_{2g} levels (d_{xy} , d_{yz} , d_{zx}) and 2 e_g levels ($d_{x^2-y^2}$, $d_{3z^2-r^2}$), and the splitting is 10 Dq . SRO has four valence electrons, thus only t_{2g} contributes and builds the valence band. Consider that the mirror plane in Fig. 4.9

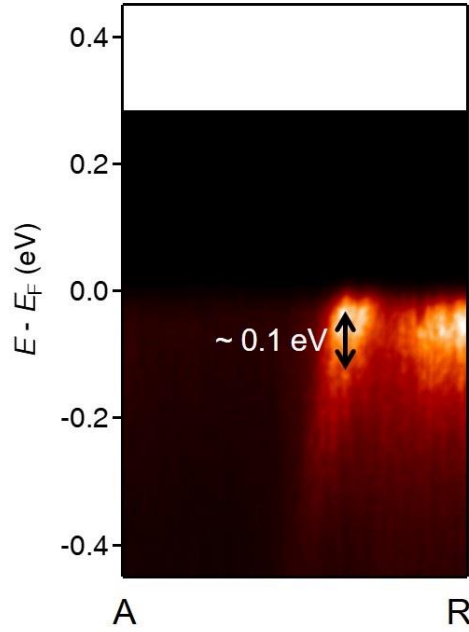


Figure 4.10 The split band observed in the FS cut shown in Fig. 4.7 (b). The energy splitting was about 0.1 eV.

is xy plane. Naturally, d_{xy} and d_{yz} are parity-odd and d_{zx} is parity-even. $M_{f,i}^{\vec{k}}$ can survive when we observe d_{xy} and d_{yz} orbital bands using s polarization (LV) and d_{zx} using p polarization (LH).

Now we could trace the orbital characters of FS-forming bands illustrated in Fig 4.8. The bright dispersion at the R point ($k_x = \pi/a = 0.8 \text{ \AA}^{-1}$, $k_y = 0$) shown in Fig. 4.6 (b) formed the strong straight-shaped FS, and its intensity was way higher when we used LH polarization. Using LV polarization, the intensity was suppressed and became comparable with other FSs. Based on the observation, we concluded that they had strong d_{zx} orbital character (and d_{yz} character at another R point, $k_x = 0$, $k_y = \pi/a = 0.8 \text{ \AA}^{-1}$).

4.3.5 Exchange splitting and its temperature evolution

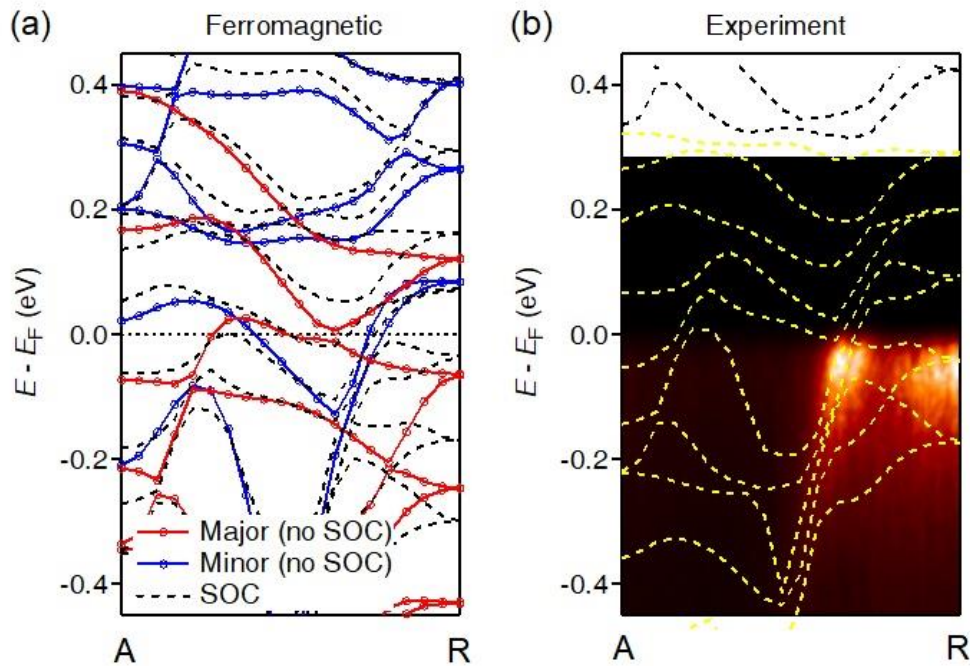


Figure 4.11 (a) LDA calculation with and without spin-orbit coupling with ferromagnetic ground state. (b) Overlapped LDA calculation. The experimental spectrum was the same with that in Fig. 4.10.

Using high resolution ARPES, we obtained the dispersion of the split bands observed in Fig. 4.7 (b). Figure 4.10 showed the band dispersion along the RA line. We observed three bands in the ARPES spectra. One was located at the R point, and it was broad (incoherent) compared with others. The others, the bright sharp split bands, were split by 0.1 eV. Though those bands were better-defined than the band at the R was, they also became incoherent when the binding energy was larger than 0.2 eV.

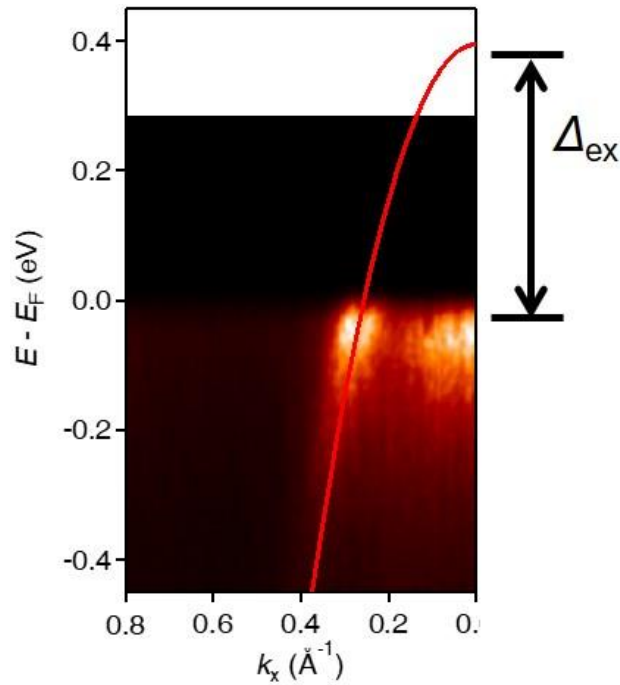


Figure 4.12 Determining Δ_{ex} in the ARPES spectrum.

We overlapped density-functional-theory (DFT) calculation based on local density approximation (LDA) to investigate origins of 0.1 eV splitting and incoherent/coherent bands. Figure 4.11 showed LDA calculation results and the experimental band dispersion with overlapped LDA calculations. Both cases that Spin-orbit coupling (SOC) was considered and not considered were shown. We also considered spin degree of freedom to reproduce the ferromagnetic ground state.

Let us have a detailed look on Fig. 4.11. In Fig. 4.11 (a), the number of valence bands larger than 4, the number of valence electrons, due to zone folding and lifted spin degeneracy by ferromagnetism. Overall, SOC did not critically change the valence band dispersions. It sometimes produced hybridization between anti-crossed bands when SOC

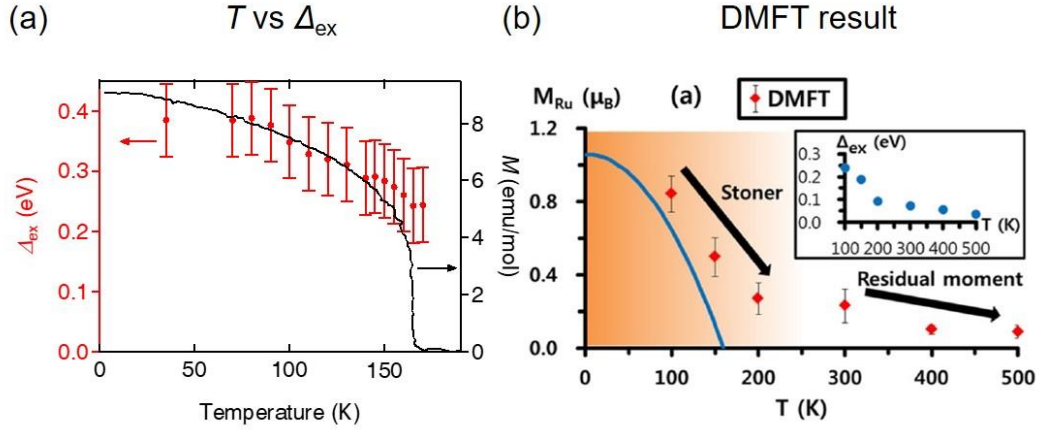


Figure 4.13 (a) T vs Δ_{ex} determined by the method described in the main text. A temperature dependent magnetization curve was referred from [5]. (b) Calculated temperature dependent magnetization and Δ_{ex} (inset). Note that Δ_{ex} did not become zero even above T_C . Adopted from [10].

was absent. Note that the small splitting observed in the ARPES spectrum was even reproduced without SOC. Thus, we could infer that the splitting possibly originated from structure distortion. However, we should remind that SOC played a role for the splitting. The splitting had been smaller than 0.1 eV without SOC. SOC increased the splitting, in order that now the size of splitting was correctly reproduced as in the Fig. 4.11 (b).

Comparing Fig. 4.11 (a) and (b), we should note that the coherent/incoherent bands had different spin characteristics. Though SOC mixed spin degree of freedom with orbital degree of freedom, at the R point, they were well separated both in energy and in momentum. It is obvious that the coherent sharp split bands and the incoherent band were remnants of spin minority band and majority band, respectively. By exploiting the spin

minority band to the R point, we could refer the exchange splitting, Δ_{ex} (refer Fig. 4.12).

By the method for experimentally obtaining Δ_{ex} in the ARPES spectrum, we obtained temperature evolution of exchange splitting in Fig. 4.13 (a). We also plotted a temperature-dependent magnetization curve for comparison. As T increased, Δ_{ex} decreased showing similar temperature dependence with scaled magnetization. However, Δ_{ex} did not become zero even above. Note that the non-zero Δ_{ex} above T_C is direct evidence of deviation from the Stoner model. Experimentally non-zero Δ_{ex} in other systems such as manganites [21] have revealed its local spin-spin interaction induced magnetic nature.

We first revealed that Δ_{ex} did not become zero even above T_C directly from experimentally obtained momentum-resolved electronic structure, and the electronic structure showed deviation from the Stoner model. Although SRO did not perfectly match with the Stoner model, the Heisenberg model either had limitation to describe the ferromagnetism of SRO. It might sound ironically, however, temperature dependence on Δ_{ex} was again strong evidence to show the second deviation. We referred a dynamic mean field theory (DMFT) result in Fig. 4.13 (b). The DMFT result reported that magnetic moment did not become zero, indicating local moment still persist above T_C , marked by *residual moment* in Fig. 4.13 (b) [10]. Though there was notable magnetic moment, magnetization below T_C followed the Stoner model. This observation was consistent with the optical spectroscopy result which suggested possibility of coexistence of local/itinerant-originated magnetic moment [8,10].

Our result was consistent with the DMFT results. First, the spin characters of incoherent/coherent bands were successfully described by DMFT before. The reason why

the spin-majority band was broader than spin-minority band is that the spin-majority band can have more channels to decay away when it is excited. Second, the temperature evolution of Δ_{ex} showed almost the same behavior. The previous ARPES report focused on an energy scale and showed that energy scale did not show changes with respect to increasing temperature. However, they did not clarify the reason for choosing the energy scale. Here, we successfully found Δ_{ex} , and observed its temperature evolution, which is the first experimental observation on evidence for dual nature of local/itinerant magnetism in SRO.

4.4 Conclusion

Importance on examination on the magnetic nature of SRO has been emphasized for a long time. Unfortunately, there had been limited experimental access to verify theoretical suggestions such as coexistence of local/itinerant magnetism. To confirm and provide critical experimental evidence to study the electronic structure of SRO, we measured 3D electronic structure by ARPES for the first time. We obtained the inner potential V_0 , which leads us to map and locate the high symmetry planes in reciprocal space. Our finding opened a way for verifying theoretical arguments. By comparing our results with calculations, we showed that the exchange splitting from ferromagnetism did not completely become zero even above the T_C . This is critical experimental evidence for the dual origin in ferromagnetism of SRO. The duality can be a consequence of local correlation as well as dynamic screening in $4d$ transition metal oxides.

References

- [1] G. Kotliar, S. Y. Savrasov, K. Haule, V. S. Oudovenko, O. Parcollet, C. A. Marianetti, *Rev. Mod. Phys.* **78**, 865 (2006)
- [2] T. Moriya, Y. Takahashi, *Annu. Rev. Mater. Res.* **14**, 1 (1984).
- [3] V. Korenman, J. L. Murray, R. E. Prange, *Phys. Rev. B* **16**, 4032 (1977).
- [4] E. C. Stoner, *Proc. R. Soc. A* **165**, 372 (1938).
- [5] N. Kikugawa, R. Baumbach, J. S. Brooks, T. Terashima, S. Uji, Y. Maeno, *Cryst. Growth Des.* **15**, 5573 (2015).
- [6] I. I. Mazin, D. J. Singh, *Phys. Rev. B* **56**, 2556 (1997).
- [7] J. S. Dodge, E. Kulatov, L. Klein, C. H. Ahn, J. W. Reiner, L. Miéville, T. H. Geballe, M. R. Beasley, A. Kapitulnik, H. Ohta, Y. Uspenskii, S. Halilov, *Phys. Rev. B* **60**, R6987 (1999).
- [8] D. W. Jeong, H. C. Choi, C. H. Kim, S. H. Chang, C. H. Sohn, H. J. Park, T. D. Kang, D.-Y. Cho, S. H. Baek, C. B. Eom, J. H. Shim, J. Yu, K. W. Kim, S. J. Moon, T. W. Noh, *Phys. Rev. Lett.* **110**, 247202 (2013).
- [9] D. E. Shai, C. Adamo, D. W. Shen, C. M. Brooks, J. W. Harter, E. J. Monkman, B. Burganov, D. G. Schlom, K. M. Shen, *Phys. Rev. Lett.* **110**, 087004 (2013).
- [10] M. Kim, B. I. Min, *Phys. Rev. B* **91**, 205116 (2015).
- [11] F. Pulizzi, *Nat. Mater.* **11**, 564 (2012).
- [12] M. Bibes, A. Marthelemy, *IEEE Trans. Electron Devices* **54**, 1003 (2007).
- [13] J. M. Rondinelli, N. M. Caffrey, S. Sanvito, N. A. Spaldin, *Phys. Rev. B* **78**, 155107

(2008).

[14] G. Herranz, B. Martinez, J. Fontcuberta, F. Sanchez, M. V. Garcia-Cuenca, C. Ferrater, M. Varela, *J. Appl. Phys.* **93**, 8035 (2003).

[15] M. Verissimo-Alves, P. García-Fernández, D. I. Bilc, P. Ghosez, J. Junquera, *J. Appl. Phys.* **93**, 8035 (2003).

[16] M. W. Haverkort, I. S. Elfimov, L. H. Tjeng, G. A. Sawatzky, A. Damascelli, *Phys. Rev. Lett.* **101**, 026406 (2008).

[17] A. Damascelli, D. H. Lu, K. M. Shen, N. P. Armitage, F. Ronning, D. L. Feng, C. Kim, Z.-X. Shen, T. Kimura, Y. Tokura, Z. Q. Mao, Y. Maeno, *Phys. Rev. Lett.* **85**, 5194 (2000).

[18] A. P. Mackenzie, J. W. Reiner, A. W. Tyler, L. M. Galvin, S. R. Julian, M. R. Beasley, T. H. Geballe, A. Kapitulnik, *Phys. Rev. B* **58**, R13318 (1998).

[19] C. S. Alexander, S. McCall, P. Schlottmann, J. E. Crow, G. Cao, *Phys. Rev. B* **72**, 024415 (2005).

[20] Y. Zhang, F. Chen, C. He, B. Zhou, B. P. Xie, C. Fang, W. F. Tsai, X. H. Chen, H. Hayashi, J. Jiang, H. Iwasawa, K. Shimada, H. Namatame, M. Taniguchi, J. P. Hu, D. L. Feng, *Phys. Rev. B* **83**, 054510 (2011).

[21] V. R. Galakhov, M. Demeter, S. Bartkowski, M. Neumann, N. A. Ovechkina, E. Z. Kurmaev, N. I. Lobachevskaya, Y. M. Mukovskii, J. Mitchell, D. L. Ederer, *Phys. Rev. B* **65**, 113102 (2002).

Chapter 5

Conclusion

Despite importance to study itinerant electron systems with photoemission spectroscopy to provide experimental electronic structures, investigations on some systems have been delayed or unexplored due to technical limitation. In this dissertation, we studied three different material systems with overcoming limitations by adopting up-to-date experimental techniques and user facilities.

First, we studied the electronic structure of Ca_2N using angle-resolved photoemission spectroscopy (ARPES). Ca_2N has been known as an electride in which electrons themselves behave as anions. we investigated the electronic structure of an electride Ca_2N by ARPES. With a couple of choices for photon energies, we could prove k_z dispersions of the electronic structure. Also, we determined that Fermi momenta k_F remained almost constant with respect to various k_z . Thus, we found that low-energy conduction should be characterized by the quasi-two-dimensional electronic structure near the Fermi level. Using various photon energies, we could determine k_z dispersion in the electronic structure, whereas the k_F values nearly remain as a constant. Hence, we confirmed that low-energy excitation or conduction governed by the electronic structure very near the Fermi level should be quasi-two-dimensional. In addition, density functional theory (DFT) calculations

showed good agreements with ARPES. The agreements supported the existence of quasi-two-dimensional anionic excess electrons suggested by DFT before our work. In conclusion, we first provided experimental evidence for the existence of the anionic excess electrons in the interstitial region in Ca_2N .

Second, we performed *in-situ* photoemission spectroscopy to study possible metallic surface states of BiO_2 -terminated BaBiO_3 (BBO) thin films. Angle-dependent x-ray photoemission spectroscopy was utilized to obtain spectral weight ratio between Ba $3d$ and Bi $4f$ core levels. From the result, we confirmed that our films had BiO_2 terminations consistent with the theoretical condition. Contrary to the prediction, no metallic surface states were observed. Surface states -3.8 eV below the Fermi level were observed from the comparison between angle-resolved valence band spectra from pristine and K-evaporated films. We concluded that detailed and accurate theoretical studies will improve description for the electronic structures of BBO.

For the last part, we first determined three-dimensional electronic structures of SrRuO_3 (SRO). There have been reports for electronic structures of SRO thin films from *in-situ* ARPES, but no ARPES from single crystalline samples was reported. From our ARPES spectra, we determined the inner potential and locate high symmetry planes which pass through the Brillouin zone center and boundary. Thus, we provided the first experimental results which can be directly compared with many theoretical calculations. We showed that the exchange splitting in the ferromagnetic state decrease as temperatures increased. However, the exchange splitting did not decrease down to zero and remained finite. This was critical experimental evidence for remnant short-range order even above the Curie

temperature and it supported coexistence of dual origin (itinerant/local) for ferromagnetism in SRO.

Appendix

Manifestations of Quasi-Two-Dimensional Metallicity in a Layered Ternary Transition Metal Chalcogenide Ti_2PTe_2

Transition-metal chalcogenides (TMCs) have attracted notable attention due to their exceptional physical properties, in addition to its high potential for application [1]. Particularly, a well-known exfoliation method has been applied to TMCs to fabricate mono- or a few-layer of single-crystalline TMCs. The exfoliated TMCs showed distinct physical properties from bulk properties [2-3] due to its low-dimensionality, especially two-dimensional (2D) characteristics. Thus, thin TMCs encouraged material scientists to study and utilize them. Most studies on TMCs have been focused on binary compounds ($TmCh_2$ composition, where Tm and Ch stands for transition metal and chalcogen ions, respectively.). Also, semiconducting compounds have attracted more attention compared to metallic compounds, since exotic ground states have been mostly predicted on semiconducting compounds [4]. $TaSe_2$ and $NbSe_2$ are rare examples of metallic compounds on which research interests focused. $NbSe_2$ showed diverse phase transition with reducing temperatures. It undergoes metal-to-superconductor transition through a charge-density-wave state [5]. $TaSe_2$ also showed similar transitions even with the modulating carrier concentration via chemical doping or intercalation [6].

Beyond the binary TMCs, single-crystalline ternary TMCs with more than two chalcogens of pnictogen and tellurium with zirconium or titanium cations were recently synthesized [7-9]. Basic building blocks of the crystals are slabs stacked with five atomic layers, showing notable difference with building slabs of $TmCh_2$. Obviously, one may expect that ternary TMCs can broaden the diversity of research interests on TMCs. One of the key characteristics of TMCs, the low-dimensionality, can be still a playground to host exotic physics. However, detailed studies on ternary TMCs have been rare so far. Specifically, electrical transport or electronic structure studies on ternary TMCs have been rarely reported.

Here, we studied the quasi-2D metallicity of a ternary TMC, Ti_2PTe_2 (TPT). We adopted both experimental and theoretical methods to investigate its transport properties and electronic structures. We measured the temperature-dependent electrical transport properties ($\rho-T$) as well as Hall coefficient (R_H). The transport results matched well with a general model of quasi-2D transport characteristic under disorders. We traced back the origin of the quasi-2D metallicity by studying its electronic structure. We mapped a FS using angle-resolved photoemission spectroscopy (ARPES). The obtained FS clearly showed two distinct features in reciprocal space. A small three-dimensional (3D) hole pocket located at the center of the first Brillouin zone (BZ) was observed, while 6 large quasi-2D electron pockets surrounded the hole pocket. We also obtained band dispersions of the hole and electron pockets and compared them with density functional theory (DFT) calculations. Both agreed well with each other.

A stoichiometric polycrystalline TPT sample was prepared from TiTe_2 and TiP by the solid-state reaction method. TiTe_2 was synthesized by mixing stoichiometric titanium and tellurium powder, and the mixture was heated in an evacuated silica tube up to $900\text{ }^\circ\text{C}$ for 24 hours. The same procedure was conducted for TiP synthesis, but the temperature was $800\text{ }^\circ\text{C}$. We synthesized TPT single crystalline samples by using NaCl flux in an alumina ampoule in a vacuum condition. TPT polycrystalline powder with NaCl powder was heated up to $1100\text{ }^\circ\text{C}$. Then the sample was slowly cooled down to $800\text{ }^\circ\text{C}$ at a rate of $1\text{ }^\circ\text{C/hr}$. Finally, the sample was cooled to room temperature by turning off the furnace. A fresh and clean surface was prepared by using two methods. The typical mechanical exfoliation method using 3M Scotch tape was applied for X-ray diffraction (XRD) and transport measurements. On the other hand, we cleaved the sample by detaching the top-post under *in situ* condition. An exfoliated single crystal of TPT was pressed onto lithographically patterned electrodes on a SiO_2/Si wafer. To prevent surface oxidation, we utilized an Ar-filled glovebox and portable glove bags during the whole sample preparation processes. We performed photoemission measurements at the 4A1 Beamline of PLS-II with a Scienta R4000 analyzer. The base pressure of an analysis chamber was below 2×10^{-11} Torr during all photoemission measurements. The sample temperature was kept at 70 K and total energy resolution was about 50 meV for ARPES. We carried out DFT calculations by adopting the full-potential linearized augmented plane-wave method, as realized in the WIEN2K package [10]. We utilized the generalized gradient approximation of Perdew, Burke, and Ernzerhof for the exchange-correlation [11]. The spin-orbit coupling was treated in the second variation.

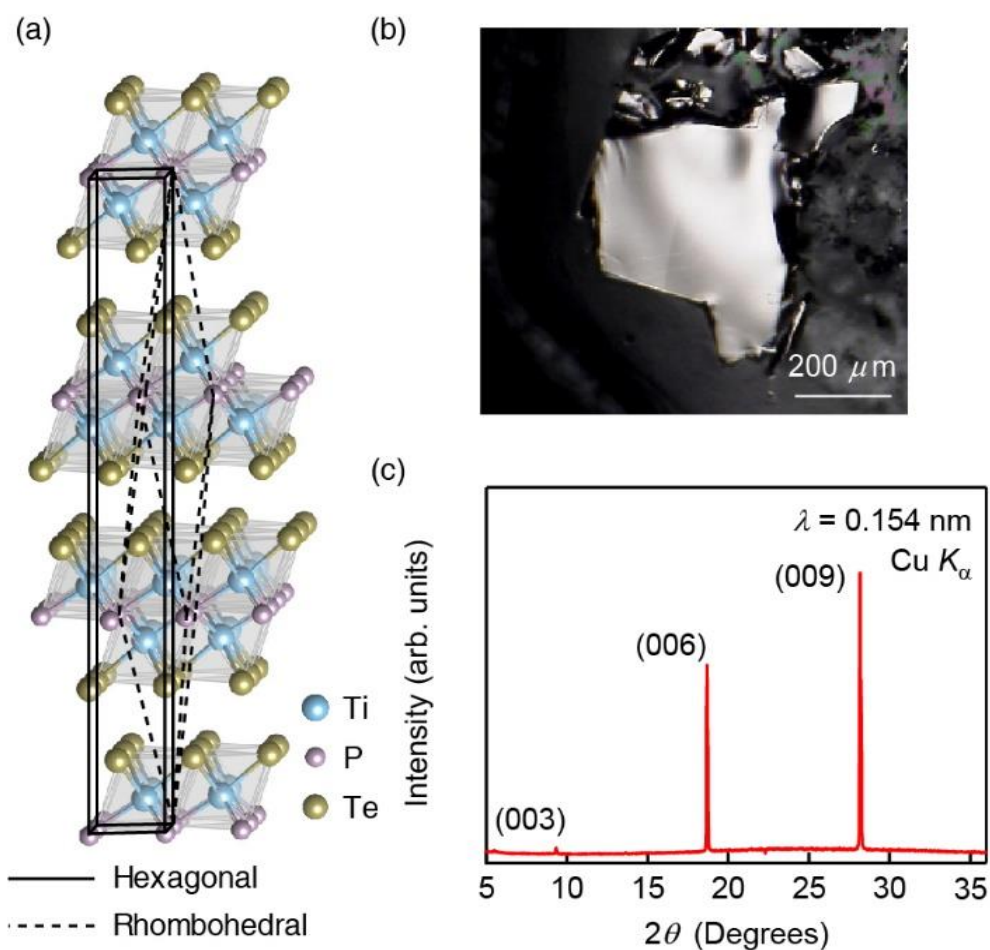


Figure A.1 (a) Crystal structure of TPT (b) Clean surface obtained by mechanical exfoliation. (c) XRD from $\lambda = 0.154$ nm radiation. Only (00 l) peaks were observed.

Figure A.1 (a) shows the crystal structure of TPT. It has a layered structure with a high c/a ratio of 7.83. The single slab of the layer unit is composed of tellurium and phosphorus as anions which are connected with titanium cations constituting the polyhedral center [7]. A unit cell consists of three slabs and van der Waals gaps, exhibiting easy exfoliation by the conventional 3M scotch tape method. As shown in Figure 1b, a plate-like crystal with a

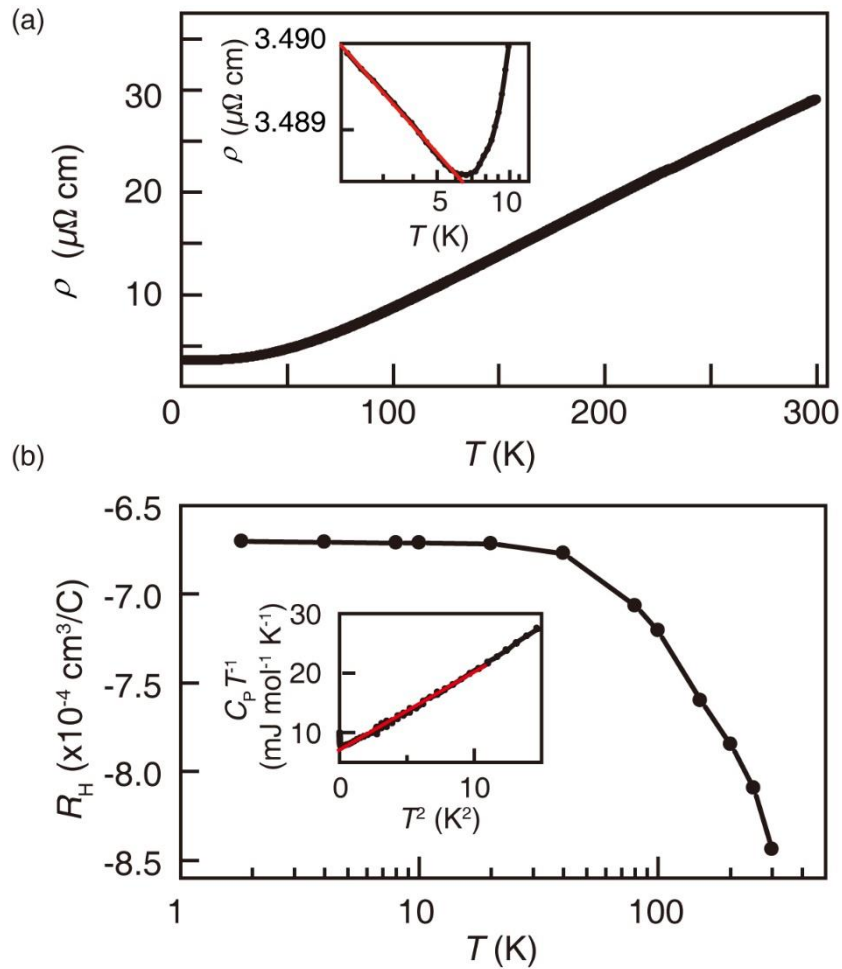


Figure A.2 (a) Temperature-dependent resistivity up to 300 K. The inset shows $\log T$ temperature dependence below 7 K. The red line is the linear fitting. (b) Temperature-dependent Hall coefficient. The inset shows CT^{-1} versus T^2 fitting from the heat capacity measurement.

shiny and clean surface was obtained with a size of $400 \times 400 \mu\text{m}^2$. Figure A.1 (c) displays the XRD pattern of the single crystalline TPT, confirming that the sample is well-oriented along the c -axis without impurity phases.

Using exfoliated crystals, we measured the T dependence of ρ along the in-plane direction. As shown in Fig. A.2 (a), the decreasing behavior of ρ was observed as T decreased from 300 to 7 K, confirming typical metallic behavior of TPT governed by electron-phonon scattering. Although TPT is a ternary compound, the ρ value at room temperature ($30 \mu\Omega\cdot\text{cm}$) is rather more comparable to that of the pure titanium metal ($43 \mu\Omega\cdot\text{cm}$) than that of TiTe_2 ($120 \mu\Omega\cdot\text{cm}$) [12-13]. Contrary to the positive slope of the $\rho - T$ curve down to 7 K, logarithmic dependence on T with a negative slope appeared below 7 K as shown in the inset of Fig. A.2 (a). The fact that logarithmic T dependence is a characteristic feature of quasi-2D systems without magnetic impurities resulting from a weak localization or electron-electron interaction [14] strongly suggests that electrical carriers in TPT transport along 2D space under a weakly disordered metallic regime.

The T dependence of the Hall coefficient (R_H) exhibits increasing behavior with the decrease in T , while the sign of R_H is negative in the measured T range, as shown in Fig. A.2 (b). This finding indicates that the primary carrier is an electron, whereas two types of carriers coexist, and the concentration ratio between electrons and holes depends on T [15]. From the heat capacity (C) measurement (the inset of Fig. A.2 (b)), the Sommerfeld coefficient value (γ) was obtained as $6.94 \text{ mJ/mol}\cdot\text{K}^2$, which is larger than those of Ti metal as well as binary metallic TMCs such as WTe_2 or MoTe_2 [16-17]. This finding implies that the 2D disordered metallic TPT shows a prominent electron-electron interaction compared to pure Ti and other TMCs, in which the phase-breaking mechanism originates in two types of carriers, as also observed in the high-stage graphite intercalation compounds containing small amounts of minority carriers [18].

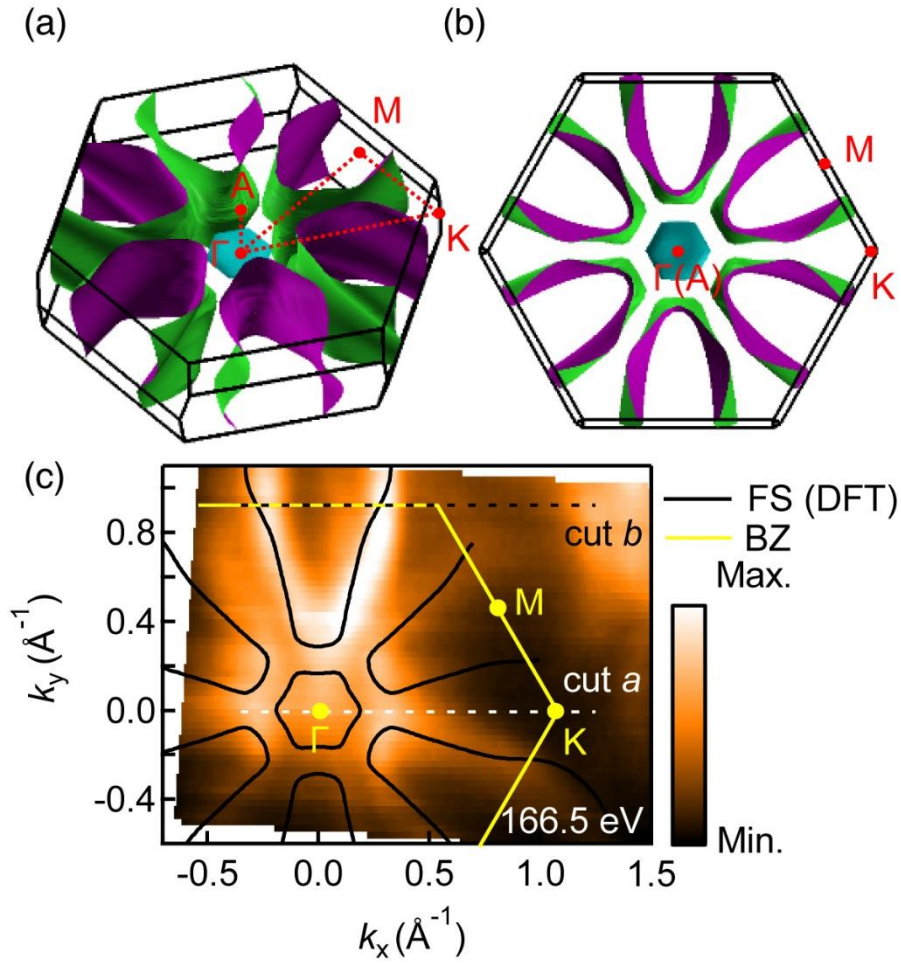


Figure A.3 (a) FSs from DFT calculations and (b) their top-view. (c) Experimental FS map from ARPES at $h\nu = 166.5$ eV. For comparison, the FSs from the DFT calculations are overlapped as black solid lines. The high symmetry points are indicated by the hexagonal zone scheme.

To investigate the origin of the metallic behavior over a range of temperature, we performed DFT calculations and ARPES measurements. Figs. A.3 (a) and (b) show the calculated FSs and their top-view, respectively. At the first BZ center, there is a small hole

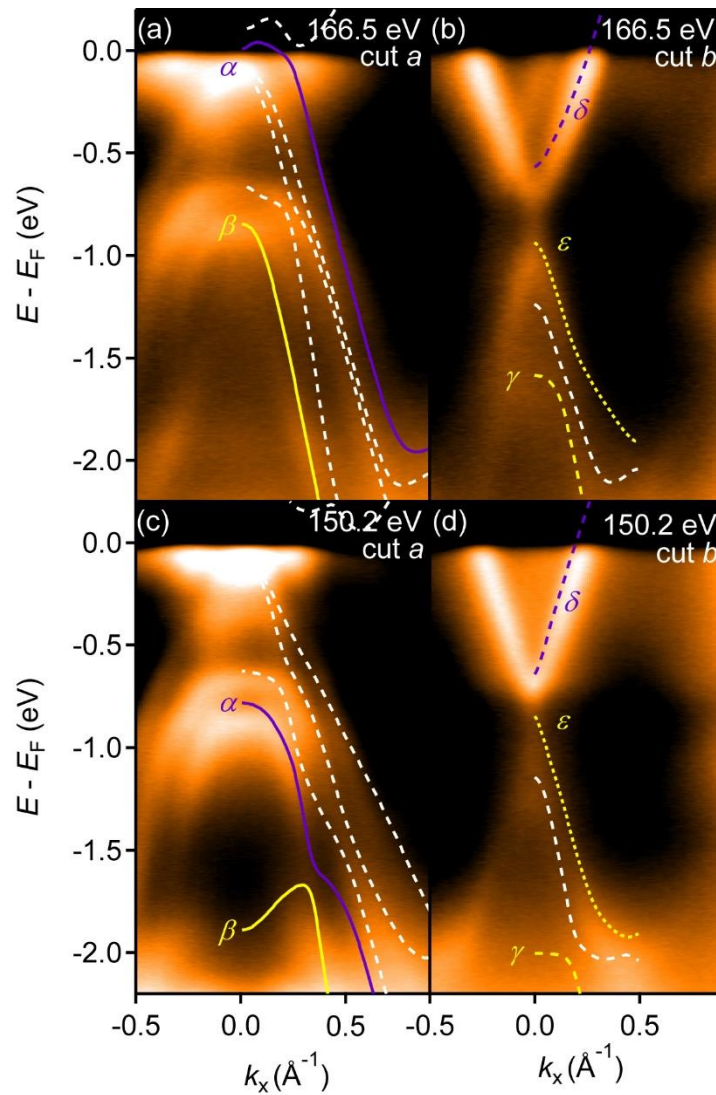


Figure A.4 ARPES spectra of TPT at $h\nu =$ (a, b) 166.5 eV and (c, d) 150.2 eV along cut a and b as indicated in Fig. A.3 (c). Overlapped solid, dashed, and dotted lines are from DFT calculations.

pocket with a hexagonal pancake shape. Six large lobe-shaped electron pockets surround the hole pocket. Note that the large electron pockets have quasi-2D characteristics except

a little warping along the k_z -axis. Since the volume of the hole pocket is negligible in comparison to that of the electron pockets, the electronic properties of TPT is dominated by the electron pockets. In addition, their quasi-2D nature is also obviously expected. The experimentally mapped FS cut at $h\nu = 166.5$ eV (the inner potential $V_0 = 10$ eV was determined by $h\nu$ -dependent ARPES measurements) is shown in Fig. A.3 (c). We overlapped the calculated FSs on the experimental FS map, and they show good agreement in their shape and sizes. The intensity differences between each electron pockets may originate from the matrix-element effect [19]. Overall, the obtained electronic structure is consistent with the transport results.

To examine the electronic structure more in detail, Figs. A.4 (a-d) present ARPES spectra and band dispersions from DFT calculations along the cuts a and b shown in Fig. A.3 (c). Two photon energies $h\nu = 166.5$ and 150.2 eV were employed to measure at the BZ center and boundary along the k_z -axis, respectively. Thus, we could investigate how the band dispersion evolves when the electron momentum increases along the out-of-plane direction. Overall, the ARPES spectra and the calculated dispersions are well matched. Slight disagreement may originate from short photoelectron escape depth. At the first glance, there seems to be little difference between the ARPES obtained at two photon energies, thus, implying the quasi-2D nature of the electronic structure of TPT.

However, a close inspection reveals several differences that may be related to the 3D characters of some dispersions and to the FS warping shown in Fig. A.3 (a). When we compare the ARPES spectra at the BZ center (Figs. A.4 (a) and (b)) and those at the BZ boundary (Figs. A.4 (c) and (d)), (1) the band forming the hole pocket in Fig. A.4 (a) (α ,

purple solid line) moves downward, thus the hole pocket disappears, and the band with near linear dispersion (β , yellow solid line) is pushed down to about -2 eV; (2) the Fermi momentum for the electron pocket decreases about 10% in the ARPES spectra and 30% in the calculated dispersion; (3) the lowest band in Fig. A.4 (b) (γ , yellow dashed line) moves downward to -2 eV, which implies that it is strongly coupled to the hole-pocket band; (4) the gap between the electron-pocket band (δ , purple dashed line) and its next lower band (ε , yellow dotted line) becomes smaller to make them look like Dirac bands. According to DFT calculations without spin-orbit coupling, they form Dirac bands, and there was an effort to move the Fermi level (E_F) to another Dirac point in the unoccupied states.⁷

If we assume the integer valences for all elements, i.e., Ti^{4+} , P^{3-} , and Te^{2-} , there is one excess electron per formula unit cell. Thus, a question naturally arises regarding where the excess electrons are located. Since the outermost shells of P^{3-} and Te^{2-} ions are completely filled, it seems to be reasonable to assume that the excess electrons mainly reside in Ti-ion sites. Then, there are two possibilities that the excess electrons are uniformly distributed in the two equivalent Ti-ion sites, or there is a charge disproportionation, i.e., an equal amount of Ti^{3+} and Ti^{4+} ions. However, we can exclude the latter because TPT is a good metal and the temperature-dependent resistivity of TPT shows no anomaly. Furthermore, there seems to be no hint of FS nesting for CDW in the FS shape. Then, the Ti $3d$ band is quarter-filled, and TPT becomes metallic even with strong correlations between Ti $3d$ electrons as in other half-filled Ti compounds [20-21].

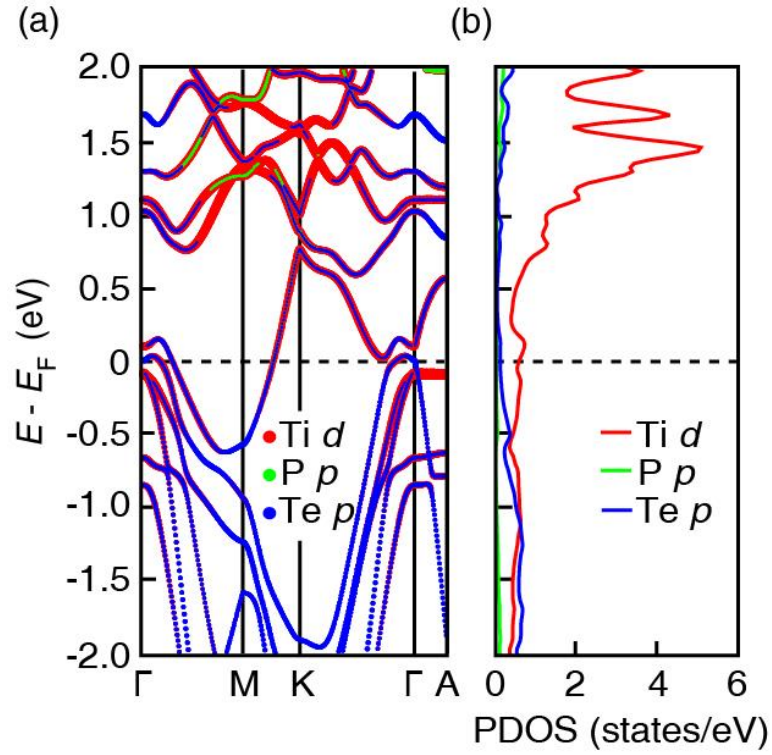


Figure A.5 (a) Orbital characters of the valence and conduction bands. (b) Partial density of states of each composing orbitals.

To confirm the character of the charge carriers in TPT, we plot the band dispersions with orbital characters for each element in Fig A.5 (a) and the partial density of states in Fig. A.5 (b). If we trace the E_F -crossing bands, we can notice that the dominating character at E_F is the Ti $3d$ orbital. Hence, Ti character determines the electrical transport properties in TPT, as inferred when considering the ionic valence states. Since the Ti ions form 2D networks, quasi-2D characteristics of transport properties are also expected. Additionally, we can see that the main character of the bands with fast dispersions along the ΓA line is the Te $5p$

orbital, which suggests that the outmost Te layers cause strong interlayer interaction, resulting in a little 3D characteristic.

In summary, we studied how quasi-2D metallicity develops in TPT and the existence of a two-band. To explore the quasi-2D nature of TPT, we analyzed the electronic structure by both theoretical and experimental approaches. FS maps confirmed the electron-governing quasi-2D nature of the electronic structure. We also demonstrated that the 2D networks of Ti ions found in the crystal structure form quasi-2D conducting channels.

References

- [1] Q. H. Wang, K. Kalantar-Zadeh, A. Kis, J. N. Coleman, M. S. Strano, *Nat. Nanotechnol.* **7**, 699 (2012).
- [2] B. Radisavljevic, A. Radenovic, J. Brivio, I. V. Giacometti, A. Kis, *Nat. Nanotechnol.* **6**, 147 (2011).
- [3] D. H. Keum, S. Cho, J. H. Kim, D.-H. Choe, H.-J. Sung, M. Kan, H. Kang, J.-Y. Hwang, S. W. Kim, H. Yang, K. J. Chang, Y. H. Lee, *Nat. Phys.* **11**, 482 (2015).
- [4] L. Perfetti, T. A. Gloor, F. Mila, H. Berger, M. Grioni, *Phys. Rev. B* **71**, 153101 (2005).
- [5] T. Yokoya, T. Kiss, A. Chainani, S. Shin, M. Nohara, H. Takagi, *Science* **294**, 2518 (2001).
- [6] K. K. Fung, S. McKernan, J. W. Steeds, J. A. Wilson, *J. Phys. C: Solid State Phys.* **14**, 5417 (1981).
- [7] F. Philipp, P. Schmidt, M. Ruck, W. Schnelle, A. Isaeva, *J. Solid State Chem.* **181**, 2859 (2008).
- [8] H. Ji, I. Pletikosić, Q. Gibson, G. Sahasrabudhe, T. Valla, R. J. Cava, *Phys. Rev. B* **93**, 045315 (2016).
- [9] K.-W. Chen, S. Das, D. Rhodes, S. Memaran, T. Besara, T. Siegrist, E. Manousakis, L. Balicas, R. E. Baumbach, *J. Phys.: Condens. Matter* **28**, 14LT01 (2016).
- [10] P. Blaha, K. Schwarz, G. Madsen, D. Kvasnicka, J. Luitz, *WIEN2k* (Karlheinz Schwarz, Techn. Universität, 2001).

- [11] J. P. Perdew, K. Burke, M. Ernzerhof, *Phys. Rev. Lett.* **77**, 3865 (1997).
- [12] R. W. Powell, R. P. Tye, *J. Less-Common. Met.* **3**, 226 (1961).
- [13] Y. Koike, M. Okamura, T. Nakanomyo, T. Fukase, *J. Phys. Soc. Jpn.* **52**, 597 (1983).
- [14] P. A. Lee, T. V. Ramakrishnan, *Rev. Mod. Phys.* **57**, 287 (1985).
- [15] H. Suematsu, K. Higuchi, S. Tanuma, *J. Phys. Soc. Jpn.* **48**, 1541 (1980).
- [16] J. E. Callanan, G. A. Hope, R. D. Weir, E. F. Westrum Jr., *J. Chem. Thermodyn.* **24**, 627 (1992).
- [17] F. C. Chen, X. Luo, R. C. Xiao, W. J. Lu, B. Zhang, H. X. Yang, J. Q. Li, Q. L. Pei, D. F. Shao, R. R. Zhang, L. S. Ling, C. Y. Xi, W. H. Song, Y. P. Sun, *Appl. Phys. Lett.* **108**, 162601 (2016).
- [18] L. Piraux, V. Bayot, J. P. Issi, M. S. Dresselhaus, M. Endo, T. Nakajima, *Phys. Rev. B* **41**, 4961 (1990).
- [19] A. Damascelli, Z. Hussain, Z.-X. Shen, *Rev. Mod. Phys.* **75**, 473 (2003).
- [20] T. Uozumi, K. Okada, A. Kotani, *J. Phys. Soc. Jpn.* **62**, 2595 (1993).
- [21] I. Hase, A. Fujimori, H. Namatame, Y. Fujishima, Y. Tokura, M. Abbate, F. M. de Groot, J. C. Fuggle, H. Eisaki, S. Uchida, *Physica B* **186**, 1074 (1993).

Publication list

- [1] Peter Lutz, Simon Moser, Young Jun Chang, Roland Koch, Soren Ulstrup, **Ji Seop Oh**, Luca Moreschini, Sara Fatale, Marco Gironi, Chris Jozwiak, Aaron Bostwick, Eli Rotenberg, Hendrik Bentmann, Friedrich Reinert, "Volatile 2D Electron Gas in Ultra Thin BaTiO₃ Films", In preparation.
- [2] **Ji Seop Oh**, Minu Kim, Gideok Kim, Han Gyeol Lee, Hyang Keun Yoo, Soobin Sinn, Young Jun Chang, Moon-sup Han, Chris Jozwiak, Aaron Bostwick, Eli Rotenberg, Hyeong-Do Kim, and Tae Won Noh, "Evidence for Absence of Metallic Surface States in BiO₂-terminated BaBiO₃ Thin Films", *Current Applied Physics* **18**, 658 (2018).
- [3] S. Moser, V. Jovic, R. Koch, L. Moreschini, **J.-S. Oh**, C. Jozwiak, A. Bostwick, E. Rotenberg, "How to Extract the Surface Potential Profile from the ARPES Signature of a 2DEG", *Journal of Electron Spectroscopy and Related Phenomena* **225**, 16 (2017).
- [4] Soobin Sinn, Kyung Dong Lee, Choong Jae Won, **Ji Seop Oh**, Moon-sup Han, Young Jun Chang, Namjung Hur, Byeong-Gyu Park, Changyoung Kim, Hyeong-Do Kim and Tae Won Noh, "Element-Specific Orbital Character in a Nearly-Free-Electron Superconductor Ag₃Pb₂O₆ Revealed by Core-Level Photoemission", *Scientific Reports* **7**, 4528 (2017).
- [5] Soobin Sinn, Choong Hyun Kim, Beom Hyun Kim, Kyung Dong Lee, Choong Jae Won, **Ji Seop Oh**, Moon-sup Han, Young Jung Chang, Namjung Hur, Hitoshi Sato, Byeong-Gyu Park, Changyoung Kim, Hyeong-Do Kim, and Tae Won Noh, "Electronic Structure of the Kitaev Material α -RuCl₃ Probed by Photoemission and Inverse Photoemission Spectroscopies", *Scientific Reports* **6**, 39544 (2016).
- [5] **Ji Seop Oh**, Ho-Sung Yu, Chang-Jong Kang, Soobin Sinn, Moon-sup Han, Young Jun Chang, Byeong-Gyu Park, Kimoon Lee, Byung Il Min, Sung Wng Kim, Hyeong-Do Kim, and Tae Won Noh, "Manifestations of Quasi-Two-Dimensional Metallicity in a

Layered Ternary Transition Metal Chalcogenide Ti_2PTE_2 ", Chemistry of Materials **28**, 7570 (2016).

[7] **Ji Seop Oh**, Chang-Jong Kang, Ye Ji Kim, Soobin Sinn, Moon-sup Han, Young Jun Chang, Byeong-Gyu Park, Sung Wng Kim, Byung Il Min, Hyeong-Do Kim, and Tae Won Noh, "Evidence for Anionic Excess Electrons in a Quasi-Two-Dimensional Ca_2N Electride by Angle-Resolved Photoemission Spectroscopy", Journal of the American Chemical Society **138**, 2496 (2016).

[8] Hyang Keun Yoo, Young Jun Chang, Luvs Mereschini, Hyeong-Do Kim, Chang Hee Sohn, Soobin Sinn, **Ji Seop Oh**, Cheng-Tai Kuo, Aaron Bostwick, Eli Rotenberg, and Tae Won Noh, "Insulating-layer formation of metallic $LaNiO_3$ on Nb-doped $SrTiO_3$ substrate", Applied Physics Letters **106**, 121601 (2015).

[9] S. B. Lee, K. Kim, **J. S. Oh**, B. Kahng, and J. S. Lee, "Origin of Variation in Switching Voltages in Threshold-Switching Phenomena of VO_2 Thin Films", Applied Physics Letters **102**, 063501 (2013).

국문 초록

물질 내 유동 전자는 전도 현상 및 자기 현상 발현과 같은 물질의 물성을 결정하는 중요한 역할을 한다. 유동 전자와 물성, 그리고 전자 구조의 관계는 알칼리, 혹은 알칼리토 금속과 같은 전자 사이 상호작용을 무시할 수 있는 간단한 물질계를 주요 대상으로 하며 발전했고 정성, 정량적인 분석을 성공적으로 진행할 수 있었다. 특히 기존 띠 이론으로 예측한 전자 구조와 실제 전자 구조에서 큰 차이가 나타났기 때문에, 전자 사이 상호작용이 큰 물질에 대한 전자 구조 연구는 상당히 까다로웠다. 이 학위논문에선 세 가지 다른 유동 전자 물질계를 광전자 분광학을 통해 연구했다. 기존의 띠 이론으로 예측했지만 실험적으로 확인할 수 없었던 내용, 혹은 기술적 한계가 있어 실제로 측정하기 어려운 물질의 전자 구조를 가속기 기반 거대 연구 시설 및 최신 실험 기법을 도입하여 연구하였다.

첫째로, 전자화물 Ca_2N 의 전자 구조 연구를 각분해 광전자 분광법을 이용해 최초로 진행했다. 전자 화물은 일반적인 이온 결합 물질과 달리 전자가 직접 음이온 역할을 한다. 방사광시설을 이용해 광자 에너지를 바꿔가며 각분해 광전자 분광 측정을 진행했고, 전자 구조의 k_z 방향 분산을 측정하였다. 전자 구조의 k_z 방향 분산 측정을 통해 페르미 모멘텀 k_F 가 k_z 값과 관계 없이 상수에 가까운 것을 발견하였다. 따라서, 전자 구조에서 페르미 준위 근방의 저에너지 영역과 밀접한 관련이 있는 전도 현상 등이 k_z 분산이 없는 준2차원의 경향을 가진다고 이해할 수 있다. 이는 밀도 함수

이론에서 예측한 것과 같은 결과이다. 이 연구 결과는 각분해 광전자 분광 실험을 통해 기존에 밀도 함수 이론 등의 이론적으로만 제시되었던 2차원 전자화물의 존재에 대한 실험적 증거를 최초로 제공하였다.

다음으로 밀도 함수 이론을 통해 예상한 BiO_2 진공/물질 경계면을 갖고 있는 BaBiO_3 페로브스카이트의 금속 표면 상태 존재에 대해 연구하였다. 이 연구를 위해 첨단 *in-situ* 각분해 광전자 분광 장비를 이용하였고, BaBiO_3 박막의 전자 구조를 실험적으로 측정하였다. $\text{Bi } 4f$ 와 $\text{Ba } 3d$ 의 핵심 전자 준위의 스펙트럼을 측정하였고, 두 스펙트럼의 세기 비율이 각도에 따라 변하는 것을 분석해 실험에 사용한 BaBiO_3 박막이 BiO_2 진공/물질 경계면을 갖고 있는 것을 확인하였다. 따라서, 금속 표면 상태가 존재할 수 있는 조건을 만족하고 있었다. 그러나 이론적으로 예측한 금속 표면 상태는 발견되지 않았다. 원자가띠 전자 구조 측정 결과는 기존 연구 결과와 일치하였다. 심층적인 연구를 위해 샘플 표면에 칼륨 원자를 증착하는 기법을 이용하였고, 이를 통해 페르미 준위 3.8 eV 아래에 표면 상태가 존재하고 있음을 발견하였다. 이 연구를 통해 BaBiO_3 의 전자 구조 연구는 기존 띠 이론에서 사용하는 근사적 방법보다 더 심층적인 연구가 필요함을 밝혔다.

마지막으로, SrRuO_3 단결정의 3차원 전자 구조를 연구하였다. 그동안 SrRuO_3 단결정을 이용해 깨끗한 절개면을 얻지 못해 각분해 광전자 분광 실험을 진행하지 못했으나, 이번 연구를 통해 최초로 SrRuO_3 의 내부 포텐셜 V_0 를 측정해 운동량 공간 내 높은 대칭성 지점에 대한 전자 구조 측정을 진행하였다. 이는 지난 20년 간 이루어진 전자 구조 연구를 검증할 수 있게 해주었다. 다양한 온도에 대해 띠 분산 측정을 진행하였고, 강자성 스핀 바꿈

에너지가 온도가 올라감에 따라 줄어드는 것을 발견하였다. 특이하게도 강자성 전이 온도에서 스핀 바꿈 에너지는 완전히 0이 되지 않고 유한한 값으로 남아 있었다. 결론적으로, 강자성 전이 온도보다 높은 온도에서도 유한하게 남은 스핀 바꿈 에너지는 스핀의 긴 범위 정렬이 사라진 이후에도 짧은 범위 정렬이 남아있음을 나타내고 SrRuO₃ 강자성에 유동/국소의 이중성을 보여주는 실험적 증거임을 밝혔다.

주요어: 유동 전자, 전자 구조, 전자화물, 2차원 전자 가스, 페로브스카이트, 유동 강자성, 각분해 광전자 분광학

학번: 2012-20373

